Advanced Materials Technologies

ADVANCED MATERIALS TECHNOLOGIES
www.advmattechnol.com

RESEARCH ARTICLE OPEN ACCESS

Two-Photon Polymerized Microvascular Environments for Multicellular Modeling of the Blood–Brain Tumor Barrier

Nastaran Barin[1,2] | Sayba Z. Chowdhury[2] | Maurice de Wit[2] | Rania Head[2] | Kiki Bals[3,4] | Erwin Brosens[3] | Marvin M. van Luijn[5] | Hayri E. Balcioglu[6] | Angelo Accardo[1] | Pim J. French[2]

[1]Department of Precision and Microsystems Engineering, Delft University of Technology, Delft, The Netherlands | [2]Department of Neurology, Erasmus MC Cancer Institute, University Medical Center, Rotterdam, The Netherlands | [3]Department of Clinical Genetics, Erasmus MC Cancer Institute, University Medical Center, Rotterdam, The Netherlands | [4]Department of Ophthalmology, Erasmus MC Cancer Institute, University Medical Center, Rotterdam, The Netherlands | [5]Department of Immunology, MS center ErasMS, University Medical Center, Rotterdam, The Netherlands | [6]Department of Medical Oncology, Erasmus MC Cancer Institute, University Medical Center, Rotterdam, The Netherlands

Correspondence: Nastaran Barin (n.barin@tudelft.nl) | Angelo Accardo (a.accardo@tudelft.nl) | Pim J. French (p.french@erasmusmc.nl)

Received: 8 December 2025 | **Revised:** 19 December 2025 | **Accepted:** 6 January 2026

Keywords: 3D-engineered scaffolds | blood–brain tumor barrier | endothelial cells | microfluidics | two-photon polymerization

ABSTRACT

Modeling the blood–brain tumor barrier (BBTB) in vitro remains a major challenge due to the structural and functional complexity of the brain microvasculature and its dynamic interactions with glioma cells. Here, we present 3D microvascular structures fabricated by two-photon polymerization (2PP) that mimic capillary architecture and enable multicellular models for studying the BBTB. Immunofluorescence and scanning electron microscopy confirm that these structures support homogenous colonization by both human umbilical vein endothelial cells (HUVECs) and human cerebral microvascular endothelial cells (hCMEC/D3), forming tubular endothelial monolayers with polarized nuclear morphology and alignment, comparable to in vivo conditions. Additionally, endothelial cells show increased expression of cytoskeletal (tubulin, F-actin) and barrier markers (ZO-1, CD31) compared to 2D cultures. The engineered model responds to TNF-α stimulation and supports co- and tri-cultures with pericytes and glioma cells. Incorporation of glioma cells leads to reduced CD31 and elevated PLVAP expression, indicating barrier destabilization. The μPCs are also integrated into commercially available microfluidic chips via in-chip 2PP, enabling stable perfusion and providing access to both luminal and abluminal sides of the endothelium. In summary, our model provides a biomimetic and adaptable platform for studying endothelial integrity, tumor-vascular crosstalk, and broad applicability in barrier biology studies.

1 | Introduction

Despite decades of intensive research, the successful translation of neuro-oncology findings into effective clinical therapies for glial brain tumors (gliomas) remains a major challenge [1–3]. A key obstacle to progress is the difficulty of therapeutics to cross the blood–brain barrier (BBB) [4]. The BBB is a selective, semi-permeable barrier that protects the brain from harmful substances while permitting essential nutrients to pass through [5, 6]. While multiple cell types contribute to its function, its primary restrictive interface is formed by tightly connected brain endothelial cells that line the brain's capillaries [7]. These endothelial cells are supported by pericytes, astrocytic end-feet, and a specialized basal lamina, which together

Angelo Accardo and Pim J. French equally supervised this work.

maintain the barrier's structural integrity and physiological role [5–8].

Brain capillaries are less permeable than other blood vessels due to the presence of intercellular tight junctions that tightly connect endothelial cells [9, 10]. In fact, more than 98% of small-molecule drugs, and nearly all large molecules, are unable to cross the BBB [10, 11]. This limits the targeting of infiltrating glioma cells, that reside behind the intact BBB, thus presenting a significant obstacle in the treatment of brain tumors [4, 12]. In addition, the BBB restricts entry of immune cells and inflammatory molecules into the brain which affects immune-based therapies [13, 14]. Besides forming a barrier for drugs and immune cells, evidence indicates that cells of the BBB actively contribute to tumor malignancy through interactions with tumor cells [15–19]. Tumor cells can remodel the BBB, forming a blood–brain tumor barrier (BBTB) that is structurally altered and partially disrupted in some areas [4, 5, 12, 20–22].

Models are therefore required to capture the complexity of the BBB and BBTB, and to enable studies of drug transport and cellular interactions [5, 23, 24]. To date several in vitro models have been developed, each with distinct advantages and limitations. Transwell models are widely used for in vitro studies, however, they lack physiological flow, 3D vascular architecture, and often fail to maintain cellular polarization [25, 26]. A more advanced approach involves chip-based models [27–29]. While these systems offer cellular polarity and controlled fluid flow, they often feature rectangular channels with diameters (typically >200 µm) [30–32] much larger than those of brain capillaries (average diameter of 7-9 µm) [33–36]. Additionally, they typically support only single (usually endothelial cells) or two cell types and when multiple cell types are included, direct cell-to-cell interactions are often limited; moreover, most chip designs provide access primarily to the luminal side of the vessel, restricting manipulation or analysis of the abluminal compartment [31, 37]. Another model that more closely mimics BBB architecture, offering realistic vessel dimensions and multicellular composition, is the gel-based model [38, 39]. However, these models often lack controlled vessel formation, the resulting vascular geometry is typically random, not easily reproducible, and fluid flow within the vessels is either absent or poorly regulated [31]. Overall, unfortunately, existing models fail to simultaneously: capture the capillary dimensions; incorporate multiple cell types; feature biomimetic microfluidic flows; create controlled vessel formation; and enable tri-dimensional cell-to-cell interactions.

To overcome these limitations, we introduce a 3D in vitro model that integrates vessel architectures with micrometric resolution, supports multicellular culture, and is compatible with microfluidic systems via in-chip fabrication, demonstrating the feasibility of perfusion-based applications. This capability has been enabled by advances in high-resolution additive manufacturing, which allows the creation of intricate 3D cell culture environments and nanometric structures, leading to physiologically relevant microenvironments for both mechanobiology and in vitro disease modeling [18, 40–45]. Among these methods, two-photon polymerization (2PP) stands out for its capacity to fabricate sub-micrometer 3D features via non-linear two-photon absorption, selectively solidifying (i.e., photocrosslinking) photosensitive materials at the laser focal point [46]. We used 2PP to create polymeric microvessel platforms with dimensions approaching those of brain capillaries and featuring a porous shell that guides tubular endothelium-like cellular organization. These 3D microenvironments enabled complete coverage of two endothelial cell lines with organized cell alignment resembling those observed in vivo and responding to TNF-α stimulation. Both pericytes and glioma cells can be incorporated into a tri-culture BBTB model, with glioma cells compromising endothelial barrier integrity. We demonstrate these structures can be incorporated into microfluidic chips, achieving full endothelial coverage under flow. Our biomimetic model thus provides a versatile microphysiological system to study the BBTB.

2 | Results and Discussion

2.1 | Design and Fabrication of Micro-Vessel Platform

The design strategy aims to use 2PP to fabricate platforms with highly precise geometries for controlled microvessel formation. The core design element is a MicroPorous tube-like Capillary scaffold (µPC, Figure 1A) that facilitates brain vessel modeling through guided cell attachment and growth on its surface. µPCs were designed with diameters ranging from 40 to 50 µm, approaching dimensions of BBB vessels (average diameter of 7–9 µm) [35, 36] and BBTB vessels (average diameters of 15–30 µm, with larger vessels observed in more proliferative tumors) [20, 34]. The pores of the µPCs are trapezoidal and vary in size, with areas ranging up to ~270 µm^2, allowing media and cells to pass through (Figure S1C–E). The µPCs are 1 mm long and composed of longitudinal and cross-sectional beams, each 3 µm thick (Figure 1A).

We fabricated the µPCs by 2PP of a methacrylate photosensitive polymer, IP-Visio, which is biocompatible and low-autofluorescent (Figure 1B,C) [47, 48]. For our initial experiments, the structures were fabricated on ITO-coated (indium-tin oxide) glass substrates (25 × 25 mm^2). Fabrication on ITO involved optimizing multiple printing parameters, such as laser power and speed. The final procedure is detailed in the Experimental Section. Each substrate contained four sets of 16 µPC structures positioned near the center of each quadrant (Figure S1). The substrate was then cut into four pieces to create four separate samples (Figure 1D). This glass-mounted format served as the basis for the static in vitro model (absence of flow), which we tested for its suitability for the formation of structured, vessel-like architectures and for supporting the sequential seeding of multiple cell types resembling those of the BBTB.

2.2 | Endothelial Organization on µPCs Under Static Culture

To evaluate the suitability of µPCs for supporting a homogenous vessel-like layer, we began by assessing endothelial cell adhesion and confluency on glass-mounted µPCs under static culture conditions. As an initial step, we used human umbilical vein endothelial cells (HUVECs) to study colonization on various (collagen coated) µPC designs. Several µPC geometries were tested (Figure S2), and the design shown in Figure 1A achieved

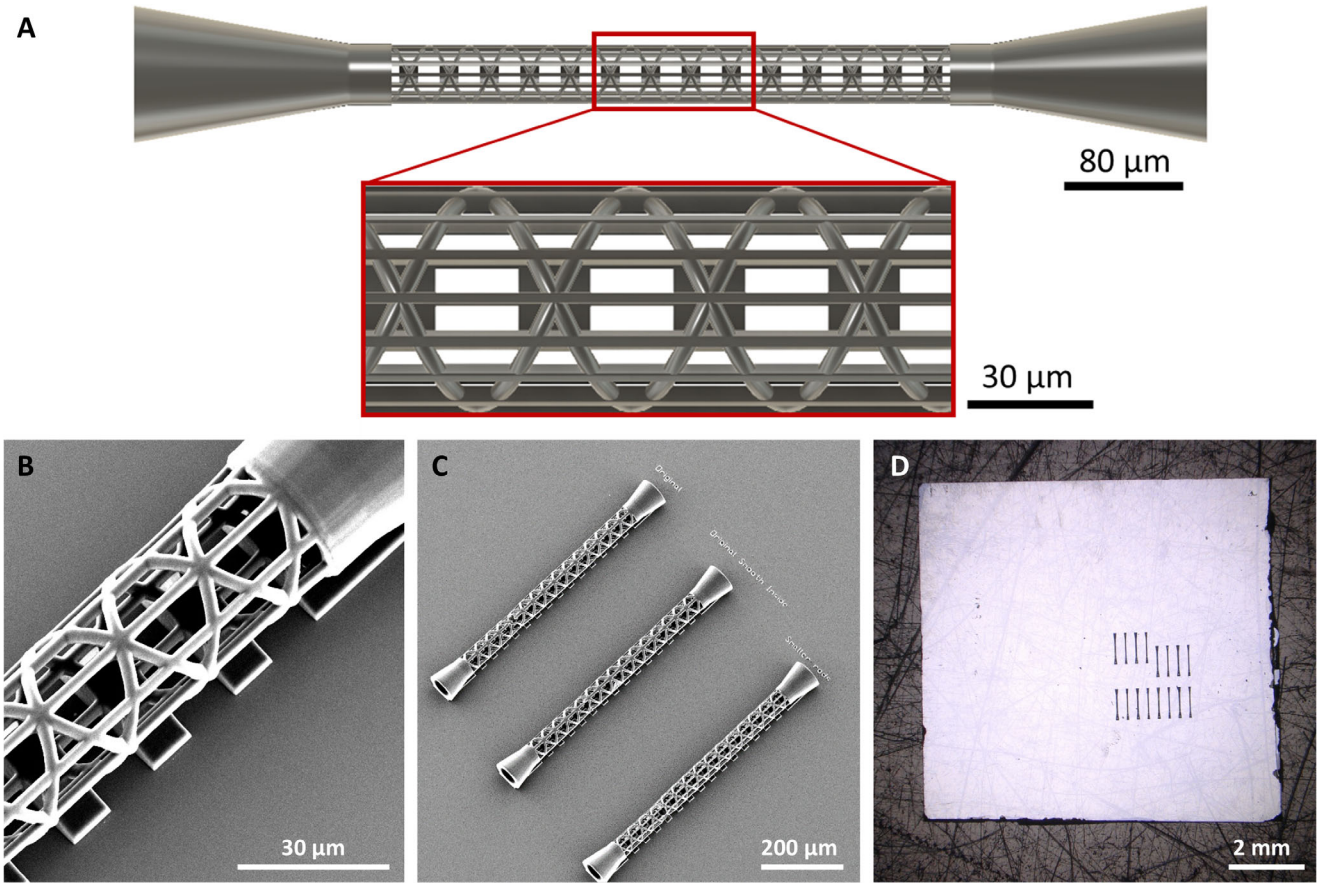

FIGURE 1 | Design and fabrication of 3D µPCs on ITO-coated glass for static culture. (A) Schematic of the 3D µPC design. (B) Zoomed-in scanning electron microscopy (SEM) image of a 2PP-fabricated µPC. (C) SEM image showing three µPCs printed on an ITO-coated glass substrate. (D) Optical image of one quarter of the substrate after sectioning, bearing sixteen µPCs (one sample set).

consistent uniform cell coverage after 3 days of culture and was therefore selected for further experiments. Despite the relatively large pore sizes of the µPCs, HUVECs successfully formed a continuous cell layer along the structures, resulting in well-organized tubular vessels (Figure 2A,B). Importantly, the more physiologically relevant human brain microvascular endothelial cells (hCMEC/D3) [49] likewise fully covered the µPCs and formed a similar tubular, capillary-like structures (Figure 2C).

The µPCs are anchored to the glass substrate, and the exposed portion of the tubular surface is fully covered by endothelial cells (a side-view SEM image illustrating the µPC-glass-cell interface is provided in Figure S3). For both cell types, a thin, uniform layer formed on the µPCs without evidence of clogging within the tubular channels (Figure 2D,E for hCMEC/D3; Figure S4 for HUVECs; Video S1 for HUVECs). There was no significant difference in endothelial layer thickness when comparing 2D cultures (6.51 ± 1.45 µm) to those grown on 3D µPCs (6.19 ± 1.53 µm, Figure 2F). It is important to note that the measured thickness of this layer likely overestimates the actual endothelial thickness, as the limited axial (Z) resolution of immunofluorescence (IF) imaging leads to signal blurring along the Z-axis. In contrast, measurements obtained by scanning electron microscopy (SEM) indicated sub-micrometer thicknesses (Figure S3), which likely underestimate the actual values, due to sample shrinkage caused by the dehydration process. Importantly, neither IF nor SEM provided evidence for multiple cell layers, and together with the measured thickness, this indicates that a thin monolayer of endothelial cells developed on the µPCs.

β-Tubulin and actin staining revealed well-organized cytoskeletal structures in endothelial cells cultured on 3D µPCs, in both HUVECs (Figure 2G) and hCMEC/D3 cells (Figure S5). Both proteins showed approximately twofold higher fluorescence intensity on the µPCs compared to adjacent 2D regions (Figure 2H,I), indicating robust cytoskeletal organization compatible with vessel-like structure formation (see Experimental Section for details on quantification procedures). The increased intensity was present both when IF expression was normalized to surface area (Figure 2H,I) and when normalized to cell count (Figure S6A,B).

Quantitative analysis revealed that cell nuclei on 3D µPCs exhibited distinct morphological differences when compared to those in 2D cultured on glass substrates (Figure 2J–P). Specifically, cell nuclei on µPCs were significantly more compact, with a smaller nuclear area of 99 ± 64 µm^2 on 3D µPCs compared to 152 ± 70 µm^2 on 2D surfaces ($p < 0.01$, Figure 2L). This 3D nuclear morphology more closely resembles the in vivo value of 78 µm^2 [50]. Such 3D nuclear organization supports a physiologically relevant chromatin architecture that can influence gene expression and cellular signaling [51, 52]. Nuclei of both endothelial cell

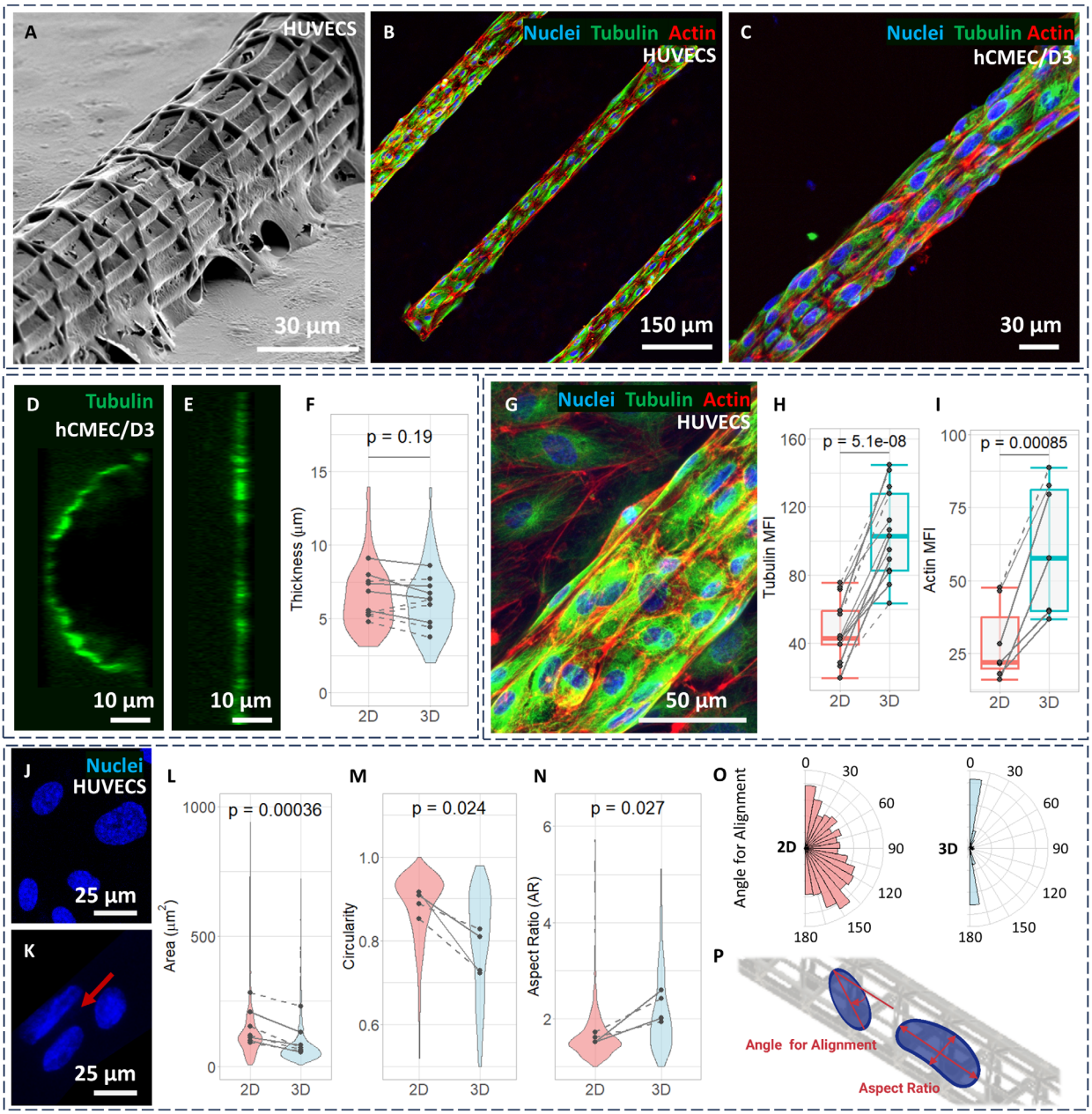

FIGURE 2 | Endothelial organization on µPCs under static culture. (A–C) Endothelial cells covering the surface of µPCs, forming tubular vessel-like structures. A) SEM image of HUVECs. (B) IF image of HUVECs. (C) IF image of hCMEC/D3 cells. (D,E) Cross-sectional IF views of hCMEC/D3 cells showing a thin endothelial layer on (D) µPCs and (E) 2D glass. (F) Endothelial layer thickness measured from IF cross-sections in both cell types. Data from 10 independent experiments ($n = 10$, $p = 0.19$); 10–24 measurements per experiment, 167 total. Solid lines represent HUVEC experiments, whereas dashed lines represent hCMEC/D3 experiments. (G–I) Cytoskeletal organization in endothelial cells on 3D µPCs versus 2D glass: (G) IF image of HUVECs showing higher fluorescence intensity of cytoskeletal markers on µPCs relative to adjacent glass. (H) Mean fluorescence intensity of tubulin for both endothelial cell types. 13 independent experiments ($n = 13$, $p < 0.001$); 2–10 paired measurements per experiment, 42 total. Solid lines represent HUVEC experiments, whereas dashed lines represent hCMEC/D3 experiments (same for I). (I) Mean fluorescence intensity of actin for both endothelial cell types. 7 independent experiments with 2 paired measurements per experiment ($n = 14$, $p < 0.001$). (J–P) Nuclear morphological differences between cells on 3D µPCs and 2D glass. (J) IF image of HUVECs on 2D glass showing flattened nuclei with random orientation. (K) IF image of HUVECs on µPCs showing elongated nuclei aligned with the longitudinal µPC axis. Only central nuclei displayed, side nuclei excluded to avoid tilt artifacts. The red arrow shows the direction of the µPC. (L) Nuclear surface area for both endothelial cell types. 7 independent experiments ($n = 7$, $p < 0.001$); 330–1712 measurements per experiment, 5559 total. Solid lines represent HUVEC experiments, whereas dashed lines represent hCMEC/D3 experiments (same for M, N). (M) Nuclear circularity for both endothelial cell types with a perfect circle having a value of 1 ($p < 0.05$). (N) Nuclear aspect ratio, indicating elongation, for both endothelial cell types ($p < 0.05$). (O) Angle between the µPC axis and the nuclear major axis, representing nuclear alignment, data normalized from four independent experiments, for both endothelial cell types. Data for (M–O): 4 independent experiments ($n = 4$); 330–1279 measurements per experiment, 2762 total. (P) Schematic illustrating the definitions of aspect ratio and alignment angle. *P* values are indicated in each figure. Panels B–C show only the 3D µPC structures (lower Z-layers omitted), whereas Panel G includes both 2D substrate cells and 3D µPC structures (full Z-stack).

types also exhibited pronounced elongation, with quantitative analysis confirming reduced nuclear circularity on µPCs ($p < 0.05$, Figure 2M). Furthermore, the nuclear aspect ratio increased significantly from a mean value of 1.59 ± 0.10 on 2D surfaces to 2.24 ± 0.31 on 3D µPCs ($p < 0.05$, Figure 2N). Notably, the aspect ratio of nuclei on µPCs closely matched the reported in vivo value of 2.23 [50, 53]. Additionally, nuclei on µPCs showed greater alignment to the longitudinal axis of the structures, whereas those on 2D surfaces showed a more dispersed alignment (Figure 2O), indicating enhanced cellular orientation and elongation even in the absence of fluid flow, resembling the natural alignment of endothelial cells along the vessel axes in vivo [54–56]. To aid interpretation, Figure 2P shows a schematic illustrating how aspect ratio and alignment angle were defined. Together, these cytoskeletal and nuclear features highlight that endothelial cells adopt in vivo-like organization on µPCs, demonstrating that 2PP-fabricated µPCs provide a biomimetic 3D platform that closely replicates the structural organization of the BBB endothelium.

2.3 | Endothelial Barrier Integrity on µPCs Under Static Culture

To establish the physiological relevance of the model, we assessed the structural integrity of the endothelial barrier formed on the µPCs, by evaluating the expression of CD31 (Cluster of Differentiation 31) and ZO-1 (Zonula Occludens-1) using IF. CD31 is an endothelial adhesion molecule, enriched at endothelial junctions, involved in maintaining cell–cell contact and vascular integrity [57]. ZO-1 is a tight junction-associated protein that seals intercellular spaces and regulates permeability by linking tight junctions to the actin cytoskeleton [58, 59]. Figure 3A,B shows robust expression of CD31 and ZO-1 on 3D µPC structures, indicating presence of endothelial junctions in HUVECs; similar results were observed in hCMEC/D3 cells (Figure S7A–C). CD31 appeared at cell–cell borders (Figure 3A; Figure S7A), and quantitative analysis revealed a significantly higher expression on the 3D µPCs compared to 2D cultures ($p < 0.01$, Figure 3C; Figure S7D). Similarly, ZO-1 was predominantly localized to cell–cell borders (Figure 3B; Figure S7B,C), and its expression was also significantly higher on the µPCs across multiple independent experiments ($p < 0.001$, Figure 3D; Figure S7E). These results support the presence of sustained endothelial barrier integrity and cell–cell adhesion in the 3D µPCs.

To further evaluate the relevance of the model, we assessed its response to inflammatory stress by exposing endothelial cells to TNF-α (Tumor Necrosis Factor-alpha), a cytokine known to disrupt tight junctions and impair BBB integrity [60, 61]. TNF-α is commonly overexpressed in gliomas and contributes to tumor progression, making it a relevant trigger for barrier disruption [62, 63]. Activation of TNF-α signaling was measured by nuclear translocation of NF-κB in hCMEC/D3 cells (Figure 3E,F). NF-κB is a key transcription factor activated during inflammatory responses and is involved in regulating genes related to barrier permeability [64, 65]. In untreated controls, NF-κB was predominantly localized to the cytoplasm (Figure 3E), whereas 24h treatment with 20 or 50 ng/mL TNF-α induced nuclear translocation (Figure 3F). TNF-α treatment resulted in a dose dependent decrease in ZO-1 expression with reduced localization at cell–cell borders (Figure 3G; Figure S8A–C). Similarly, actin filament density was diminished (Figure 3H; Figure S8D–F). Despite these effects, cells cultured on 3D µPCs retained higher levels of ZO-1 and actin intensity compared to 2D cultures under both treatment conditions (Figure 3G,H). Since conventional TEER and permeability measurements are not compatible with this static configuration due to the microscale dimensions of the µPCs and the lack of physically separated luminal and abluminal compartments, we instead leveraged this setup for high-resolution immunofluorescence imaging and mechanistic assessment of cell–cell interactions.

2.4 | Establishing Multicellular BBB Complexity on µPCs under Static Culture

To evaluate the versatility of the µPC static platform and its relevance for modeling the BBTB, we co-cultured glioma cells onto endothelialized µPCs. To verify that glioma cells can adhere to and grow on the µPCs, and that the structure's geometry is not a limiting factor, we first cultured the U87 human glioblastoma (grade 4 glioma) cells directly on the structures without the presence of an endothelial layer. U87 cells successfully attached and grew on the µPCs (Figure S9), confirming glioma-µPC compatibility. We then performed the co-culture experiments and after three days of culturing endothelial cells (HUVECs or hCMEC/D3) on the µPCs, glioblastoma cells were added sequentially and incubated for an additional three days. To distinguish between the two cell types, CD31 was used as a marker for endothelial cells. While glioma cells were identified using GFAP (Glial Fibrillary Acidic Protein), a well-established intermediate filament marker commonly expressed in gliomas, or using S100 (S100 calcium-binding protein), which is frequently upregulated in glial-origin tumors [66, 67]. Figure 4A shows a typical example of a co-culture of glioma cells (GFAP-positive) with endothelial cells (CD31-positive, HUVECs), both covering the structures. Similar results were observed with hCMEC/D3 cells (Figure S10A).

Endothelial cells (CD31-positive HUVECs or hCMEC/D3) co-cultured with U87 cells in 2D showed regions lacking a CD31 signal, consistent with endothelial detachment or local loss of coverage, suggesting compromised adhesion and reduced structural stability. In contrast, HUVECs on 3D µPCs maintained more cohesive coverage and exhibited higher CD31 IF intensity compared to the 2D monolayer condition (Figure 4B,C). Similar results were observed for hCMEC/D3 cells (Figure S10B). Quantification confirmed significantly higher CD31 intensity on 3D µPCs for both endothelial cell types ($p < 0.01$, Figure 4D). This may reflect the more physiologically relevant architecture of the µPCs, which facilitates cell–cell interactions and promotes tubular organization and cell adhesion, factors known to support endothelial maturation and stabilize junctional proteins such as CD31.

Despite the higher baseline expression levels of CD31, endothelial cells showed reduced CD31 IF intensity after the addition of glioma cells compared to controls cultured without gliomas. This effect was observed both in hCMEC/D3 cells (Figure 4E,F) and in HUVECs (Figure S11). Quantification confirmed a significant reduction in CD31 intensity for both endothelial cell types ($p < 0.01$, Figure 4G), suggesting that glioma cells can disrupt

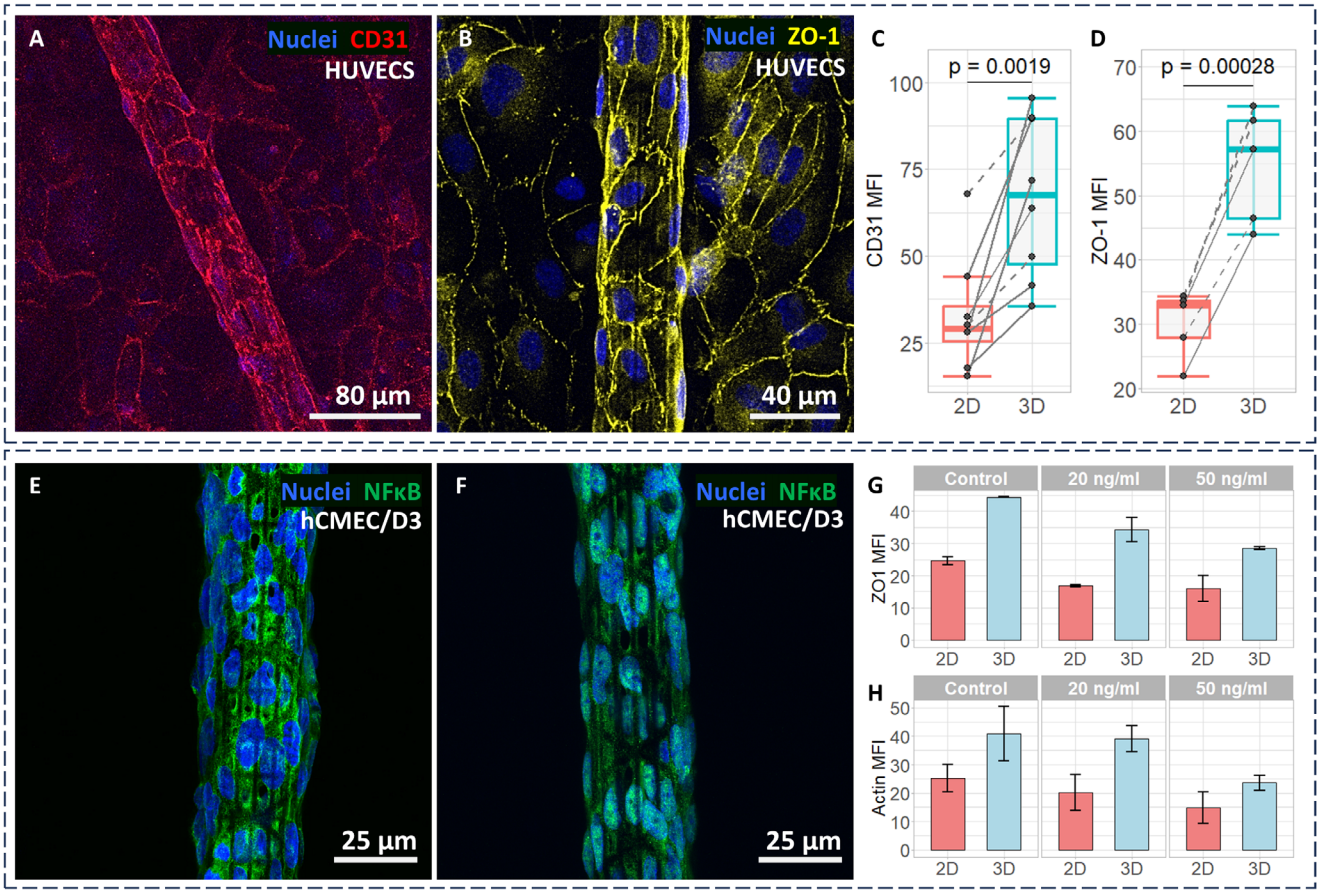

FIGURE 3 | Endothelial barrier integrity on µPCs under static culture. (A–D) Endothelial cells cultured on a 3D µPC and adjacent 2D glass. (A) IF image of CD31 expression in HUVECs, indicating presence of junctions. (B) IF image of ZO-1 in HUVECs, also indicating junction formation. (C) Mean fluorescence intensity of CD31 on 3D µPCs compared to adjacent 2D glass for both endothelial cell types. Data from 8 independent experiments ($n = 8$, $p < 0.01$); 2 paired measurements per experiment, 16 total. Solid lines represent HUVEC experiments, whereas dashed lines represent hCMEC/D3 experiments (same for D). (D) Mean fluorescence intensity of ZO-1 on 3D µPCs compared to adjacent 2D glass for both endothelial cell types. Data from 5 independent experiments ($n = 5$, $p < 0.001$); 2 paired measurements per experiment, 10 total. (E-H) TNF-α–mediated disruption of endothelial cells. Data are from two independent experiments (n = 2), one with HUVECs and one with hCMEC/D3. (E) NFκB localized to the cytoplasm in untreated hCMEC/D3 controls. (F) NFκB translocated to the nuclei following treatment with 50 ng/mL TNF-α in hCMEC/D3 cells, confirming pathway activation. (G) ZO-1 fluorescence intensity decreased after 24 h of TNF-α exposure in both endothelial cell types. (H) Actin fluorescence intensity similarly reduced over 24 h of TNF-α exposure in both endothelial cell types. P values are indicated in each figure. Panels A–B include both 2D substrate cells and 3D µPC structures (full Z-stack), whereas Panels E–F show only the 3D µPC structures (lower Z-layers omitted).

endothelial identity and compromise BBB integrity even on the µPCs [17, 68]. In line with this, previous studies report that while CD31 is often still detectable in tumor-associated vessels, its localization is frequently altered, with signal redistributed to the cytoplasm and showing focal loss along the vessel wall [69, 70]. To further demonstrate that glioma cells mediate endothelial disruption on µPCs, we examined the expression of plasmalemma vesicle-associated protein (PLVAP), a marker of fenestrated and permeable endothelium that is commonly upregulated under pathological conditions, including glioma-associated vasculature [71]. PLVAP IF intensity was compared between HUVECs endothelial-only controls and co-cultures with U87 glioblastoma cells. In the absence of glioma cells, PLVAP expression remained low (Figure 4H). However, in U87-HUVECs co-cultures, PLVAP levels were markedly increased (Figure 4I), showing an approximately 2.7-fold rise in mean fluorescence intensity relative to the controls (Figure 4J). The reduced CD31 and increased PLVAP levels suggest that the presence of glioma cells can disrupt this stability and compromise barrier function on µPCs.

To further assess whether the µPC platform can support multi-cellular cultures, we next incorporated pericytes, which play a critical role in regulating BBB integrity, vascular stability, and structural maturation [72, 73]. Pericytes alone could adhere and spread on the structures, confirming cell-scaffold compatibility (Figure S12). To evaluate their structural contribution in a multicellular context, pericytes were added after an initial 3-day culture period of human brain microvascular endothelial cells (hCMEC/D3) on the µPCs and then the cells were co-cultured for an additional 2 days. Platelet-Derived Growth Factor Receptor-Beta (PDGFR-β) was used as a marker for pericytes [74]. The results indicate that while CD31-positive endothelial cells densely cover the µPC structures, PDGFR-β-positive pericytes are also present but are more sparsely distributed (Figure 4K; Figure S13A), which is consistent with their localization in the

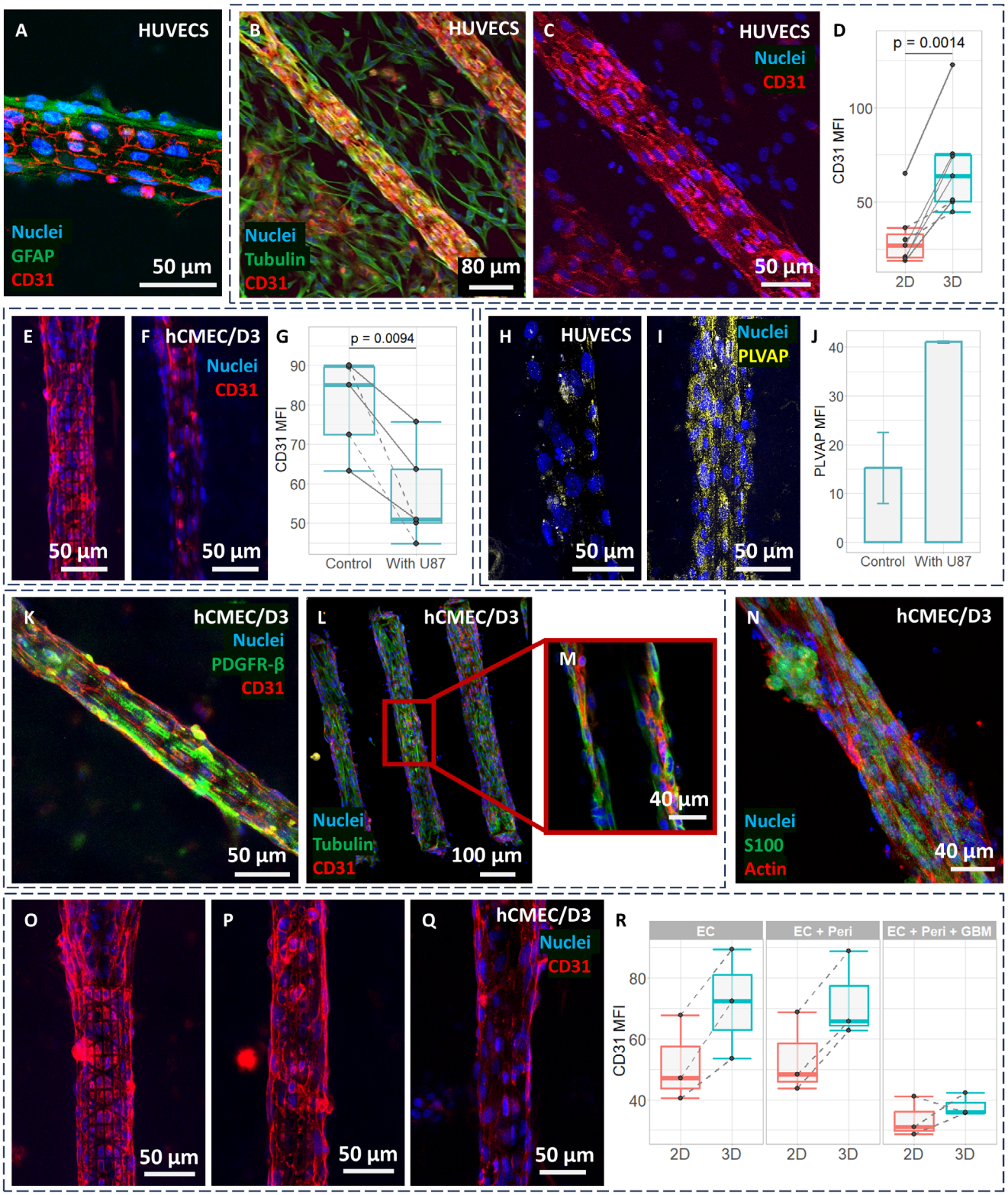

FIGURE 4 | Endothelial barrier integrity on µPCs under static culture. (A) Co-culture of U87 glioma cells (GFAP-positive) with HUVEC endothelial cells (CD31-positive) on µPCs. (B-D) CD31 expression remained higher in endothelial cells co-cultured with glioblastoma cells on µPCs compared to adjacent glass. (B) Overview IF image of HUVECs and U87 cells. (C) Zoomed-in IF view showing CD31 in HUVECs co-cultured with U87 cells. (D) Mean fluorescence intensity of CD31 for both endothelial cell types. Data from 7 independent experiments ($n = 7$, $p < 0.01$); 2–6 paired measurements per experiment, 22 total. Solid lines represent HUVEC experiments, whereas dashed lines represent hCMEC/D3 experiments. (E-G) CD31 IF intensity in endothelial cells, showing reduced expression after co-culture: (E) hCMEC/D3 monoculture control. (F) hCMEC/D3 and U87 co-culture. (G) Mean fluorescence intensity of CD31 for both endothelial cell types. Data from 5 independent experiments ($n = 5$, $p < 0.01$); 4–8 measurements per experiment, 24 total. Solid lines represent HUVEC experiments, whereas dashed lines represent hCMEC/D3 experiments. (H-J) PLVAP IF intensity in endothelial cells, showing increased expression after co-culture: (H) HUVECs monoculture control. (I) HUVECs and U87 co-culture. (J) Mean fluorescence intensity

vascular network [74, 75]. A single Z-slice IF image (Figure 4L,M) shows multiple cells stacked on top of each other along the µPC structures, showing layered cell organization (Figure S13B).

To further enhance the complexity of the BBTB model, we established a tri-culture system comprising endothelial cells (hCMEC/D3), pericytes, and glioma cells (U87) (Figure 4N). The cells were introduced sequentially: endothelial cells were cultured for three days, followed by the addition of pericytes for two days, and finally U87 glioma cells for an additional three days. CD31 expression was assessed across three conditions: endothelial monoculture, endothelial-pericyte co-culture, and endothelial-pericyte-glioma tri-culture (Figure 4O–R). Confocal imaging and quantitative analysis showed comparable CD31 intensity between monoculture and co-culture conditions, indicating that pericyte addition did not disrupt endothelial integrity (Figure 4P). However, the introduction of glioma cells resulted in a decrease in CD31 intensity, similar to what was observed when co-culturing endothelial cells with U87 cells (Figure 4G) showing glioma-mediated disruption of endothelial junctions, also in the presence of stabilizing pericytes (Figure 4Q).

In summary, these multicellular co-culture experiments demonstrate that our model system has a physiologically relevant architecture and enables controlled investigation of tumor-endothelium interactions. This is particularly relevant to the invasive front of gliomas, where endothelial and tumor cells are closely associated [76, 77].

2.5 | Fabrication and Integration of µPCs into Microfluidic Devices

To explore the potential for dynamic cell culture applications, we integrated 2PP-fabricated µPCs and support structures directly into commercially available microfluidic chips. This integration was carried out using two different types of microfluidic chips (Figure 5A,B). The first type is a single-channel chip that allows direct flow inside the µPCs (Figure 5A), where endothelial cells and culture medium are introduced via the same channel. The second type is a dual-channel chip in which the µPCs are 3D printed at the intersection of two perpendicular channels (Figure 5B). In this configuration, one channel enables internal fluid flow through the µPCs, exposing the inner surface of endothelial cells to media under physiological flow conditions. The second channel provides access to the external surface of µPCs and is used to introduce endothelial cells. This setup also allows future expansion to include drugs or additional cell types (Figure 5C). Both setups required the fabrication of supporting walls with circular openings that served as inlets for the µPCs, guiding the direction of flow (Figure S14). In single-channel chips, 18 to 22 µPCs with diameters of 40–50 µm were incorporated (Figure 5D–G), while in dual-channel chips, the reduced working space allowed fabrication of 8 to 12 µPCs with 40 µm diameters (Figure 5H–J).

To ensure stable integration of the µPCs within both chip types, additional fabrication considerations were necessary. To optimize adhesion and polymer/surface detection, surface functionalization through plasma treatment and silanization was enhanced compared to the preparation of standard ITO substrates. Printing directly on the chip was prone to bubble formation due to localized overheating, therefore, the laser power at the interface (the first 6 µm) was reduced by 10% compared to the upper regions of the structures (for details see the Experimental Section). Additionally, achieving proper alignment of the prints within the chip was of high importance. Initial localization of the chip-resin interface was performed manually by observing optical feedback from the 2PP setup software. After identifying the approximate interface region, the 2PP setup's automatic detection precisely located the interface for each structure, compensating for substrate unevenness and ensuring consistent adhesion. The laser focal position on the XY plane relative to the live camera was identified by printing a small cross, with the cross center defining the origin of the laser reference frame. This point was then aligned, using the live camera, to the central position of the microfluidic chip, establishing a new reference origin for the system, after which all subsequent prints were automatically aligned accordingly.

For both chip types, the fabrication process involved two steps (Figure S15). Initially, the structures were printed directly inside the microfluidic chips, using a 'dip-in laser lithography' (DiLL) configuration with the 25× objective immersed in IP-Visio within the chip. Following this step, the chip was sealed by gluing a coverslip to its edges while IP-Visio remained inside the channel. In the second step, using an 25× oil immersion objective (objective placed outside of the closed chip) and IP-Visio filled inside the chip, the top and lateral surfaces of the support walls were printed to complete the sealing process. Due to differences in geometry between the single- and dual-channel chips, the sequence of printing the support structures and main components varied. Detailed fabrication protocols for each configuration are provided in the Experimental Section and Supplementary Materials (Figures S15 and S16). Printing entirely in oil immersion mode was not feasible for two main reasons. First, interface detection at the chip bottom was unreliable in oil mode because it frequently resulted in inaccurate focusing, chip surface damage, or detachment of printed structures. Second, the working distance of the 25× oil immersion objective (WD: 380 µm) was a limiting factor

of PLVAP. Data are from two independent experiments (n = 2), both with HUVECs. (K) Pericyte (PDGFR-β-positive) and hCMEC/D3 endothelial (CD31-positive) co-culture on µPCs. (L,M) Layered organization of hCMEC/D3 endothelial–pericyte co-culture on µPCs: (L) Maximum projection of Z-stack showing overall 3D structure, and (M) Single Z-slice, zoomed-in view. (N) Tri-culture of U87 glioma cells (S100-positive), hCMEC/d3 endothelial cells, and pericytes on µPCs, with all cells stained for actin. (O-R) CD31 IF intensity in (O) hCMEC/D3 endothelial monoculture, (P) hCMEC/D3 endothelial-pericyte co-culture, showing sustained CD31 levels, and (Q) hCMEC/D3 endothelial-pericyte-glioma tri-culture, showing reduced CD31 levels. (R) Mean fluorescence intensity of CD31 in hCMEC/D3 cells. Data from 3 independent experiments ($n = 3$); 6–18 measurements per experiment, 30 total. Solid lines represent HUVEC experiments, whereas dashed lines represent hCMEC/D3 experiments. P values are indicated in each figure. Panels B–C include both 2D substrate cells and 3D µPC structures (full Z-stack), whereas Panels A, E–F, H–L, and N–Q show only the 3D µPC structures (lower Z-layers omitted).

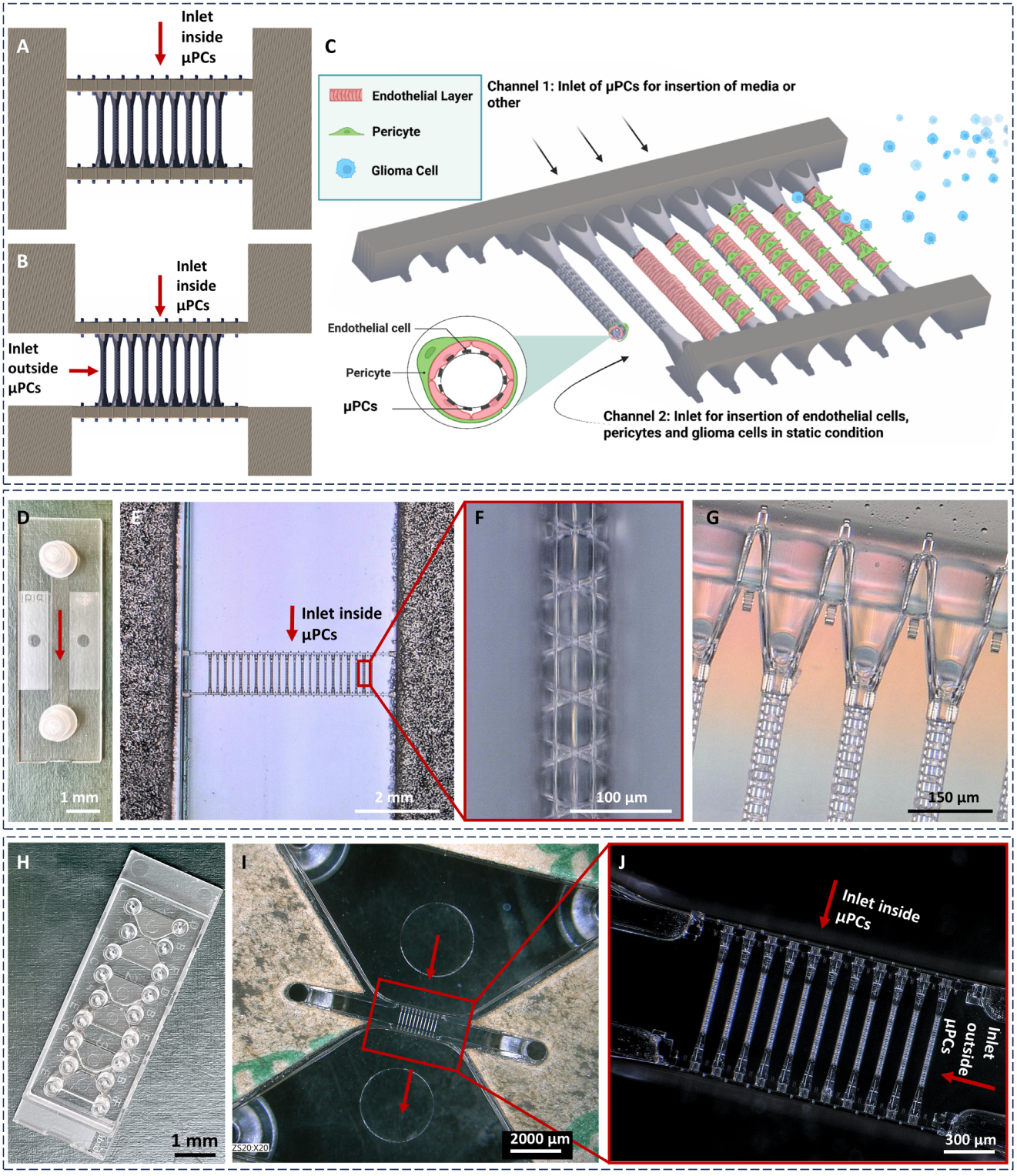

FIGURE 5 | Fabrication and integration of µPCs into microfluidic devices. (A) Schematic of a single-channel chip with direct flow through the interior of the µPCs. (B) Schematic of a dual-channel chip with two perpendicular channels: one channel enables internal fluid flow through the µPCs, and the other channel provides access to the exterior surface of the µPCs. (C) Schematic of a dual-channel chip design showing the capability for extension to support multicellular cell cultures. (D) Image of a single-channel chip, with a red arrow showing the direction of flow. (E) Optical image of the 2PP-fabricated µPCs and the supporting walls within the single-channel chip, with a red arrow indicating the direction of flow. (F) Zoomed-in optical image of the µPCs fabricated within a microfluidic chip. (G) Zoomed-in optical image of the µPCs connected to the supporting walls, featuring the inlets to the µPCs. (H) Image of a dual-channel chip. (I) Optical image of the 2PP-fabricated µPCs and the supporting walls within the dual-channel chip, with a red arrow indicating the direction of flow. (J) Zoomed-in optical image of the 2PP-fabricated µPCs and the supporting walls within the dual-channel chip, with a red arrow indicating the two inlets.

for accessing deeper regions. The two-step printing approach was able to overcome these limitations, enabling successful *in-chip* fabrication.

2.6 | Endothelial Cell Culture Under Dynamic Flow Conditions

To validate the suitability of the integrated μPCs for supporting vascular cell culture, we assessed their ability to support endothelial monolayer formation under dynamic flow. HUVEC cells were introduced into single-channel chips and cultured under physiologically relevant flow using a pressure-driven pump with a feedback sensor, operating in the μL/min range (Figure S17). In brain capillaries and small arteries, shear stress typically ranges from ~1–15 dyn/cm^2 [78–80]. To approximate these conditions, our μPCs (40-50 μm diameter) were operated under continuous flow at 12 μL/min in single-channel chips and 5 μL/min in dual-channel chips. Under these conditions, the resulting wall shear stresses inside each μPC were ~7.8 dyn/cm^2 and ~6.5 dyn/cm^2 for the single- and dual-channel configurations, respectively (Figure S18), well within the physiological microvascular range. Importantly, the corresponding Reynolds numbers remained below 1 ($Re < 1$), indicating that flow throughout the main channels and μPC lumens is strictly laminar with no turbulence or recirculation (Figure S18). The cells were allowed to adhere and proliferate over the course of three days, and all flow experiments were performed in a humidified incubator at 37°C and 5% CO_2. After three days of perfusion under biomimetic flow conditions, HUVECs uniformly colonized the surfaces of the μPCs, with IF imaging confirming cellular attachment and μPCs coverage (Figure 6A–D; Figure S19).

A dual-channel setup offers greater flexibility and functionality as it enables independent access to the space surrounding the μPCs, which is essential for introducing additional cell types, administering drugs, or measuring permeability. Furthermore, in the single-channel configuration, air bubbles occasionally became trapped in the μPC region and without external access to this compartment, could not be removed effectively, which required the experiment to be restarted. We therefore also tested our μPCs in such a dual-channel setup with either HUVEC or hCMEC/D3 endothelial cells. The cells were introduced through the outer channel surrounding the μPCs rather than through their interior, which reduced the number of cells required for seeding. IF imaging confirmed that HUVECs uniformly covered the μPC surfaces in the dual-channel chip configuration as well (Figure 6E–G), with CD31 expression indicating the formation of intercellular junctions and endothelial identity (Figure 6G). Human brain microvascular endothelial cell line (hCMEC/D3) also demonstrated complete coverage of the μPCs with cells exhibiting healthy morphology (Figure 6H).

These results demonstrate that 2PP-fabricated μPCs can be *in-chip* manufactured within commercially available microfluidic platforms, compatible with high-resolution IF imaging, and support endothelial monolayer formation under biomimetic flow conditions. Compared to existing in vitro models, the μPC platform offers several distinct advantages. Unlike conventional microfluidic chip-based systems, it provides capillary-scale vessel dimensions and direct access to both the luminal and abluminal sides of the endothelium. In contrast to gel-based models, the μPC design enables highly controlled and reproducible vessel architecture with consistent flow dynamics. Furthermore, incorporating the 2PP-fabricated structures into commercially available microfluidic chips represents a key technical advancement. This approach merges the precision and design flexibility of 2PP fabrication with the efficiency and reproducibility of standardized platforms.

Building on these advantages and on prior benchmarks from functionally validated under-flow 2PP-printed BBB [37] and BBTB [81] models, we adopt a complementary design strategy that prioritizes scaffold architecture, optical accessibility, and biological modularity while maintaining compatibility with future perfusion-based implementations. Several architectural and material features distinguish our μPC platform from prior models [37, 81]. By intentionally developing the μPC platform with stepwise complexity, we demonstrate that 2PP-fabricated microvessel scaffolds can serve as stand-alone 3D culture systems under static conditions. The larger pore openings in the tubular mesh enable direct cell–cell contact across the scaffold wall and facilitate high-resolution visualization of endothelial morphology and junctional organization. In addition, the use of a low-autofluorescence photoresist significantly improves immunofluorescence imaging quality compared with earlier approaches. The incorporation of pericytes further expands the biological relevance of the model. Finally, the in-chip 2PP fabrication within commercially available microfluidic platforms significantly reduces fabrication burden and improves accessibility, providing a practical pathway toward future flow-enabled BBTB studies.

3 | Conclusion

This research presents a 3D-engineered microvascular platform, fabricated via 2PP, for in vitro modeling of the BBTB. The platform features microporous, capillary-like structures (μPCs) with dimensions approaching native brain microvasculature, enabling complete endothelial coverage, improved nuclear morphology, cytoskeletal organization, and expression of key barrier markers. The μPCs enable multi-cellular culture under static conditions and can be integrated via *in-chip* printing within microfluidic environments, where we demonstrate compatibility with endothelial models. We show that our model supports stable tri-cultures of endothelial cells, pericytes, and glioma cells, recapitulating critical aspects of barrier integrity and tumor-induced disruption. The integration into commercially available microfluidic chips demonstrated confluent endothelial coverage, supporting the platform's compatibility with dynamic culture systems, and suggesting its potential as a versatile foundation for advanced BBTB modeling.

The μPC model was intentionally developed with stepwise complexity to support initial testing and optimization and the structures readily function as a scaffold platform under static culture conditions. However, to develop a more complete model under flow, key functional validations remain to be assessed, including assessments of basal lamina formation, [15, 82] vessel permeability [39, 81, 83, 84], and transendothelial electrical resistance (TEER) [83, 85–87], which are critical to fully establishing barrier integrity and functionality. To more accurately

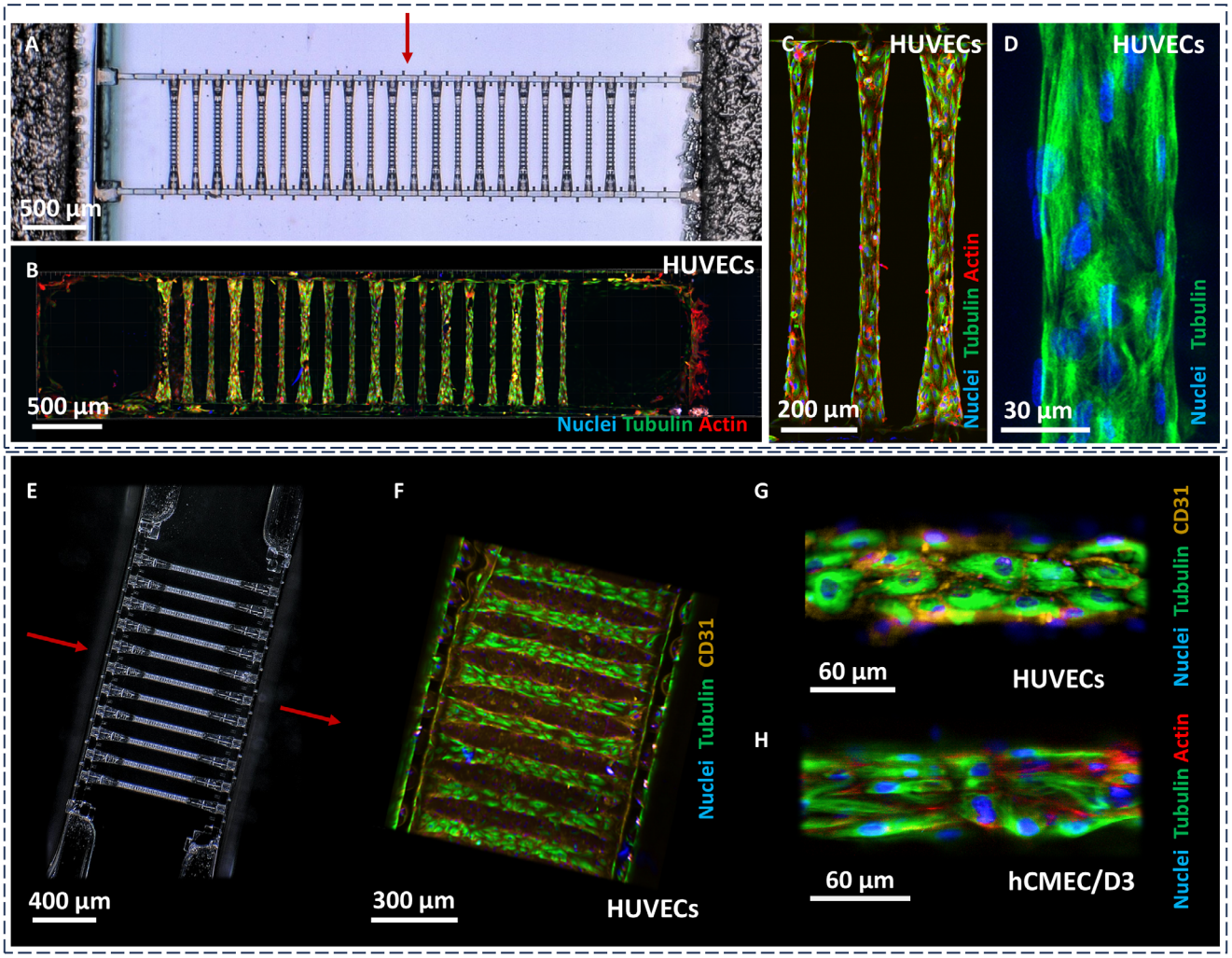

FIGURE 6 | Endothelial cell culture on 2PP-fabricated µPCs under dynamic flow. (A) Optical image of the µPC array integrated into a single-channel microfluidic chip; the red arrow indicates flow direction. (B-D) HUVECs cultured on µPCs under flow in the single-channel chip: (B) IF overview of the full µPC array. (C) IF view of three µPCs. (D) Zoomed-in IF view of a single µPC. (E) Optical image of the µPC array in a dual-channel microfluidic chip; the red arrow indicates flow direction. (F-H) Endothelial cells cultured on µPCs under flow in the dual-channel chip: (F) IF overview of the µPC array with HUVECs. (G) Zoomed-in IF view showing HUVEC coverage of µPC surfaces with CD31 staining. (H) Zoomed-in IF view showing hCMEC/D3 coverage of µPC surfaces with actin staining. Panels B–G show only the 3D µPC structures (lower Z-layers omitted).

replicate the BBTB, future work should incorporate pericytes and glioma cells alongside endothelial cells within the microfluidic system under physiologically relevant flow. In addition, the model could further evolve into a more comprehensive neurovascular unit by including astrocytes and immune cells (e.g., microglia) [88, 89]. Finally, future investigations incorporating permeability assays and therapeutic testing can further strengthen the model's translational potential in brain tumor research.

4 | Experimental Section

4.1 | µPC Design and File Preparation

The µPCs and the supporting wall structures were designed using Autodesk Fusion 360, a Computer-Aided Design (CAD) software. Following the design phase, the models were exported in Standard Triangle Language (STL) format. The STL file was then imported into DeScribe software (Nanoscribe, Germany) to establish and optimize the printing parameters. Subsequently, the General Writing Language file generated from DeScribe was imported into Nanowrite, the dedicated printing software for the Nanoscribe 2PP printer.

4.2 | µPC Fabrication on ITO Glass for Static Culture

µPCs were fabricated with the 2PP method using a Photonic Professional GT+ printer (Nanoscribe, Germany). This was carried out using Dip-in Laser Lithography (DiLL) configuration with a 25× objective featuring a 0.8 numerical aperture. IP-Visio, a methacrylate-based negative tone photosensitive polymer (Nanoscribe, Germany), was applied to indium-tin oxide (ITO)-coated glass substrates measuring 25 × 25 × 0.7 mm (Nanoscribe, Germany). Before printing, ITO-coated glass substrates were cleaned with 2-propanol (IPA, Sigma-Aldrich) and treated with oxygen plasma (Diener Femto plasma etcher) for 15 min at 80 W

with 5 sccm O_2 flow and 0.12 bar pressure. Substrates were then silanized using 2% v/v 3-(trimethoxysilyl) propyl methacrylate (MAPTMS, Sigma Aldrich) in ethanol for 1 h to promote bonding with the 2PP resin. The substrates were subsequently washed with ethanol and allowed to dry. A drop of IP-Visio was applied to the center of each substrate. The IP-Visio resin was then polymerized using a 780 nm femtosecond pulsed laser (full power equal to 50 mW). After parameter optimization, final μPCs were fabricated using a scan speed of 10 000 μm s^{-1}, 60% laser power (30 mW), and hatching and slicing distances of 0.5 μm. Stitching was implemented to accommodate the limited scan range of the galvanometric mirrors by dividing the μPCs into smaller units (Figure S20). Optimal overlap between stitched units was 5 μm in XY and 5 μm in Z with a stitching angle of 20°. After fabrication, the samples were chemically developed in propylene glycol monomethyl ether acetate (PGMEA, Sigma-Aldrich) for 30 min, rinsed with IPA for 5 min, and air-dried under a chemical fume hood. Each ITO substrate contained four sets of sixteen μPC structures, printed near the center of each quadrant of the square substrate. The substrates were scribed into four sections using a diamond-tipped scribing wheel (The PELCO FlexScribe 200, Ted Pella) and then separated along the scribe lines and transferred into 12-well cell culture plates (CLS3513-50EA, Corning).

4.3 | μPC Fabrication on Microfluidic Chips for Dynamic Flow Culture

For single-channel and dual-channel chips, a sticky-Slide I Luer (81128, channel height 0.1 mm, Ibidi, Germany) and a sticky-Slide Chemotaxis (80328, Ibidi, Germany) were utilized, respectively. These bottomless channel slides feature an adhesive underside (50 μm adhesive height) that allows for the mounting of substrates, in this case, coverslip (24 × 50 mm^2, 170 μm thick). The chips and the coverslip were placed in a plasma etcher (Diener Femto plasma etcher) and underwent oxygen plasma treatment for 20 min at a power setting of 80 W, with an oxygen flow rate of 5 sccm and a pressure of 0.16 bar. Following this treatment, 100% MAPTMS (Sigma-Aldrich) was applied inside the channels, and the coverglass was placed in 2% v/v MAPTMS in ethanol for 1 h to facilitate silanization. Channels and coverglass were then rinsed with ethanol and air-dried.

Similar to ITO glass-mounted prints, the 2PP printing was conducted using the Photonic Professional GT+ printer (Nanoscribe, Germany) with a 25× objective, utilizing IP-Visio material. An in-house built sample holder was 3D printed to accommodate the chips in the 2PP printer (Figure S21). To correct for substrate rotation around the Z-axis, the stage coordinate system was recalibrated by selecting two points along the chip edge to define a new X-axis. This alignment was then used in the 2PP software to apply a matrix transformation and realign the printing plane.

A drop of IP-Visio resin was applied to the center of the microfluidic channel, and the initial print sequence was performed using the DiLL configuration. For single-channel chips, this included printing the supporting walls and μPCs. After printing, the gap between the chip side walls and the supporting walls was manually sealed. The chip was then removed from the printer, the adhesive cover was peeled off, and a coverglass was placed while IP-Visio remained in the channel. Subsequent printing was performed using the oil-immersion configuration, during which the tops of the supporting walls were sealed by printing rectangular blocks (Figure S22). These blocks were easily adjustable in size, as they were generated from code rather than STL files, avoiding additional steps for parameter adjustments. The sequence of printing steps is depicted in Figure S15A.

For dual-channel chips, the DiLL and oil-immersion configurations were used differently than in the single-channel workflow (Figure S15B). In this case, the DiLL configuration was used only to print rectangular blocks that would later serve as sealing elements for the supporting walls. Subsequently, the chip was returned to the printer, and the main components, μPCs and supporting walls, were printed in the oil-immersion configuration. These structures were fabricated starting from the glass substrate and extending upward toward the top of the chip. This modification was required by the geometry of the chemotaxis channels (Figure S23). Video S2 presents the outcome of this two-step printing procedure recorded with the Nanoscribe camera, alternating focus between the top and bottom layers.

For the supporting walls, a scan speed of 50 000 μm s^{-1}, 80% laser power (40 mW), 1 μm slicing, and 0.5 μm hatching, and a stitching angle of 20° were used. Overlap between stitched units was 5 μm in XY and Z. μPCs were printed at 10 000 μm s^{-1}, 70% laser power (35 mW), with 0.5 μm hatching and slicing, and a stitching angle of 24° with overlap of 6 μm in both XY and Z. For both μPCs and supporting walls, the initial 10 layers near the substrate interface were printed at reduced laser power to prevent substrate damage, 56% for μPCs and 70% for supporting walls, while maintaining the same scan speed. Rectangular sealing blocks were printed at 75 000 μm s^{-1}, 100% laser power (50 mW), with 1 μm slicing and 0.5 μm hatching. The initial 10 layers near the substrate interface were printed at a scan speed of 50 000 μm s^{-1}, 80% laser power (40 mW). For sealing blocks printed in the oil-immersion configuration, the laser power was gradually increased with each layer at a slope of 0.025. After fabrication, samples were developed in IPA for 2 h, then rinsed sequentially with Novec, IPA, and 100% ethanol (1 min each), and air-dried under a chemical fume hood.

4.4 | Microfluidic Setup

Single-channel chips were directly connected to microfluidic silicone tubing (10841, ID 0.8 mm, Ibidi) using male Elbow Luer Connectors (10802, Ibidi). For dual-channel chips, the inlets were not compatible with Ibidi Elbow Luer Connectors, therefore, inlet tubing (silicone tubing ID 3.2 mm, Saint-Gobain Tygon) was first glued to inlets using UV-curable adhesive (NOA 81, Norland Optical Adhesive) and cured under 405 nm UV light, 70% power for 5 min (LED Cube 100 IC, Hönle group, maximum irradiation intensity 30,000 mW/cm^2). The attached tubing was then connected to Elbow Luer Connectors, which were subsequently linked to the main silicone tubing (10841, ID 0.8 mm, Ibidi). Because the Ibidi's chip design included two inlets and two outlets, a Y-connector was used to merge the inlets and outlets into single tubing lines (Figure S24). Before each experiment, all tubing was rinsed with 70% ethanol and then flushed with fresh media to ensure sterility and remove residual ethanol.

Flow rate was controlled using a pressure-based flow controller (LineUp Flow EZ 345 mbar, Fluigent) in combination with a flow rate sensor (Flow Unit M, range 0–120 µL/min, Fluigent). The flow was set to 12 µL/min for single-channel chips and 5 µL/min for dual-channel chips, regulated through a feedback loop between the sensor and controller. Liquid media was pressurized in a reservoir (50 mL Falcon tube with pressure cap, P-CAP50-HPPCK, Fluigent) and directed toward the chip. Both the reservoir and microfluidic chip were housed in an incubator to maintain controlled temperature and humidity (Figure S24). The media exiting the system was collected in a waste Falcon tube. After 2 days, it was manually replenished by mixing at a 1:2 ratio with fresh media and reintroduced into the reservoir.

4.5 | Cell Culture

Human Umbilical Vein Endothelial Cells (HUVECs) from pooled donors were acquired from Lonza Biosciences (Catalog Number: C-2519A). For initial setup optimization, HUVECs from pooled donors obtained from PromoCell (Catalog Number: C-12203) were used. The HUVECs were cultured in Endothelial Growth Medium (EGM-2, Lonza), which comprises Endothelial Basal Medium EBM-2 (C-3156, Lonza), supplemented with 2% Fetal Bovine Serum (FBS) and EGM-2 Supplements (C-4176, Lonza). Human cerebral microvascular endothelial cells (hCMEC/D3) were cultured in Microvascular Endothelial Growth Medium (EGM-2 MV, Lonza), which was composed of Endothelial Basal Medium EBM-2 (C-3156, Lonza) with 5% FBS and EGM-2 MV Microvascular Endothelial Cell Growth Medium supplements (C-4147, Lonza). For both endothelial cell types, culture flasks were coated with 5% collagen type I (Sigma # C9791) diluted in Hank's Balanced Salt Solution (HBSS, Gibco #14170) for a duration of 1 h. Following the coating process, the flasks were washed twice with phosphate-buffered saline (PBS, 21040CV, Corning) prior to the seeding of cells. To maintain cell cultures, the culture medium was replaced every 48 h, and the cells were subcultured upon reaching 90-100% confluency using Trypsin/EDTA (0.05%, 25300054, Gibco, USA).

Pericytes were acquired from Innoprot (P10363) and cultured in Innoprot Pericyte Medium (P60121). The medium was supplemented with 2% FBS, 1% Pericyte Cell Growth Supplement, and 1% Penicillin/Streptomycin solution, all sourced from Innoprot. Flasks were coated with 2 µg/cm^2 of Poly-L-Lysine for 1 h.

Human glioblastoma cell line U87 was cultured in Dulbecco's Modified Eagle Medium (DMEM, 41966029, Gibco, USA), supplemented with 10% fetal bovine serum (FBS) and 1% Penicillin/Streptomycin solution.

4.6 | Cell Seeding for Static Culture

Each sample was positioned in a well of a 12-well cell culture plate (CLS3513-50EA, Corning). The samples underwent sterilization using 2 ml of 70% isopropanol for a duration of 5 min, followed by two washes with 2 ml of PBS. Subsequently, the samples were coated with 5% collagen. A total of 0.8×10^6 cells (HUVECs or hCMEC/D3) were seeded into one well atop each sample, and 2 ml of fresh medium was added to the well. The cells were permitted to grow on the samples for a period of 3 days. In the co-culture models with glioblastoma, 0.7×10^6 U87 cells were seeded onto the pre-formed endothelial layer after 3 days of endothelial cell culture. The models were maintained in EGM-2 and cultured for an additional three days.

In the co-culture of endothelial cells and pericytes, 0.25×10^6 pericytes were seeded onto hCMEC/D3 endothelial cells after three days of endothelial culture and maintained for an additional two days. The co-culture medium consisted of one-third Innoprot pericyte medium and two-third MV EGM-2 medium. In the tri-culture model, U87 cells were added to the pre-established hCMEC/D3 endothelial-pericyte co-culture. A total of 0.7×10^6 U87 cells were seeded and sustained for an additional three days. The media for the tri-culture model also comprised one-third Innoprot pericyte medium and two-thirds MV EGM-2 medium to support optimal growth conditions.

4.7 | Cell Seeding for Dynamic Flow Culture

To ensure complete wetting and air removal from the microstructures, channels were initially filled with 100% ethanol due to its low surface tension. Ethanol was then gradually diluted with sterile water, followed by a gradual exchange to 5% collagen type I (Sigma-Aldrich, C9791) diluted in HBSS (Gibco, 14170) and incubated for 1 h. Afterward, the appropriate cell culture media was introduced into all channels. Endothelial cells were suspended at 2×10^6 cells/mL, and approximately 60,000 cells were seeded into single-channel chips and 20,000 cells into the middle channel of dual-channel chips using 20 µL pipettes. After seeding, cells were allowed to attach without flow for 1 h for single-channel chips and 3 h for dual-channel chips under standard incubator conditions (37°C, 5% CO_2). Following attachment, the tubing was connected to the chips and constant flow was applied at 12 µL/min for single-channel and 5 µL/min for dual-channel chips. Throughout flow culture, chips were maintained inside the incubator.

4.8 | Treatment with TNF-α

Tumor Necrosis Factor, TNF-α (Gibco-PeproTech, 300-01A-50UG, human recombinant), was introduced at concentrations of 20 ng/ml and 50 ng/ml for a period of 24 h.

4.9 | Immunofluorescence Staining

The fixation and staining procedures were similar for both static and microfluidic setups. For the static condition, all steps were performed in 12-well plates. For the microfluidic setup, the chip was disconnected from the pump, and inlet tubing was removed using tweezers. All subsequent steps were performed manually by pipetting solutions into the channels: 200 µl for dual-channel chips and 1 ml for single-channel chips.

Cells were fixed with 4% paraformaldehyde and permeabilized with 0.1% Triton X-100. After blocking in 1% bovine serum albumin (BSA), samples were incubated with primary antibodies

for 1.5 h at room temperature. The primary antibodies utilized were: Beta-tubulin (Abcam, ab6046, dilution 1:200), CD31 (Cell Marque Antibodies, 131M-95, dilution 1:50), ZO-1 (Invitrogen, 33-9100, dilution 1:100), NF-kB p65 (Abcam, ab32536, dilution 1:200), GFAP (DAKO, Z0334, dilution 1:200), S100 (DAKO, Z0311, dilution 1:200), PDGFR-β (Cell Signaling, 3169, dilution 1:100), and PLVAP (Abcam, ab81719, dilution 1:50).

Secondary antibody incubation was performed for 1 h using Alexa Fluor 488 anti-rabbit (Life Technologies, A11008), Alexa Fluor 488 anti-mouse (Abcam, ab150113), Alexa Fluor 568 anti-mouse (Life Technologies, A10037), and Alexa Fluor 633 anti-rabbit (Life Technologies, A21072), diluted 1:500 in PBS with 1% BSA, selected according to the species of the primary antibody. Additionally, F-actin was labeled with Alexa Fluor 647-phalloidin (Invitrogen, A22287, dilution 1:200).

For dynamic flow cultures, Hoechst (Molecular Probes, 33258, 1:2000 in PBS) was introduced into the channels and incubated at 4°C overnight, then replaced with PBS prior to imaging. For static cultures, two imaging setups were used: samples mounted under a coverslip, and samples imaged while submerged in media, each influencing the final preparation steps. For the mounted imaging setup, an imaging spacer (120 µm thickness, GBL654002, Grace Bio-Labs, USA) was placed on top of the sample to protect the µPCs from the coverslip (24 × 50 mm^2, 170 µm thick). Samples were then mounted with VECTASHIELD HardSet Antifade Mounting Medium with DAPI (H-1500-10, Vector Laboratories, USA), covered with a glass coverslip (24 × 50 mm^2, 170 µm thick), and stored at 4°C for 2 days before imaging. In the submerged imaging setup, Hoechst (1:2000 in PBS) was added to the wells at 4°C for a minimum duration of 2 days, after which it was replaced with PBS prior to imaging.

4.10 | Confocal Microscopy

For static experiments, two confocal imaging setups were used: samples mounted under a coverslip and samples imaged while submerged in media (Figure S25A–C). For the mounted imaging setup, the Confocal Stellaris 5 LIA system (Leica Microsystems, Germany) was used. Images were acquired using a 20× air objective (NA 0.75, Figure S25A) and a 40× oil immersion objective (NA 1.3, Figure S25B). The acquisition involved sequential excitation to avoid spectral overlapping between channels. For the submerged setup, a Dragonfly 200 upright spinning disk confocal microscope (Andor) equipped with a 25× water-dipping objective (NA 1.1, Nikon) was used. Samples were immersed in PBS during the acquisition (Figure S25C). For both imaging setups, Z-stacks were acquired with a 1 µm step size and a resolution of 2046 × 2046 pixels.

For dynamic flow experiments with single-channel chips, imaging was performed using the Dragonfly 200 with a 25× water-dipping objective (NA 1.1, WD 2mm, Nikon), using the previously described settings (Figure S25D). For dual-channel chips, an increased working distance was necessary because of the different printing process employed, where the prints started from the glass and extended upward toward the chip (Figure S19). Therefore, the Dragonfly 200 was used with a 10× air objective (NA 0.45, WD 4 mm, Nikon, Figure S25E) and a 40× water dipping objective (NA 0.8, WD 3.5 mm, Nikon, Figure S25F), selected for their large working distances.

Z-stacks were acquired to capture both cells on the 2D substrate and cells on the 3D µPC structures. In some representative images, the full Z-stack (including both layers) is shown, whereas in others only the upper Z-stack corresponding to the 3D µPC structures is displayed. The specific representation used is indicated in each figure legend.

4.11 | Scanning Electron Microscopy

SEM was performed to evaluate the quality of the printed µPCs and to assess endothelial cell coverage in static cultures. For preparations of samples containing cells, the cells were rinsed twice with PBS and fixed in 2.5% glutaraldehyde for 2 h at room temperature. Following a PBS rinse, the samples were dehydrated through a graded ethanol series (30%, 50%, 70%, 90%, and 100%), with each step lasting 5 min. Dehydration was completed using a graded series of hexamethyldisilazane (HMDS) in ethanol (25%, 50%, 75%, and 100%, 5 min each). Residual HMDS was allowed to evaporate overnight before imaging [45].

To prevent charge accumulation during imaging, samples were coated with a gold nanolayer using a JEOL JFC-1300 sputter coater (Tokyo, Japan). Each sample was coated once in a horizontal orientation (20 mA, 20 s), followed by two additional coatings at opposing 45° angles (20 mA, 10 s each) to ensure uniform gold coverage [47]. SEM imaging was performed using a JEOL JSM-6010LA scanning electron microscope (Tokyo, Japan). Secondary electron images were acquired at accelerating voltages ranging from 10 kV to 15 kV, with a beam spot size of 40 nm.

4.12 | Optical Microscopy

For quality control of 2PP structures fabricated inside chips, a Keyence VHX digital microscope was used in coaxial illumination mode, equipped with ZS-20 (20×–200×) and ZS-200 (20×–200×) monochrome objectives.

4.13 | Image Analysis

Fluorescent images were analyzed using ImageJ software (National Institutes of Health, USA). Macrocodes were created to extract and quantify the relevant features from each image. All analyses were conducted on Z-projections generated from confocal stacks. To minimize artifacts from the 3D geometry of the µPCs, only the central area of each µPC, where cells were positioned in the image plane, was analyzed, while the peripheral curved regions were excluded to avoid signal distortion caused by tilt (Figure S26). In experiments comparing IF intensity between 2D and 3D culture conditions, measurements were performed within the same image by analyzing the µPC region relative to the adjacent 2D glass region. When comparing experimental conditions, background fluorescence was subtracted uniformly, and comparisons were made using images acquired under identical imaging parameters from the same independent experiment.

Protein expression from IF images was evaluated using two complementary methods. In the first method, fluorescence intensity was normalized by area: mean fluorescence intensity (MFI) was calculated as the sum of pixel intensities within each region of interest divided by the area. In the second, fluorescence intensity was normalized by cell number: raw integrated density, defined as the sum of pixel intensities within a region of interest, was measured and then divided by the corresponding nuclei count for each region.

Nuclear segmentation and counting were performed using the StarDist plugin [90]. To analyze cellular morphology on μPCs, only cells located within the central region of the μPC were included. The aspect ratio (AR) was calculated to quantify nuclear elongation, defined as the ratio of the major axis to the minor axis of an ellipse fitted around each nucleus (AR = major axis / minor axis). Circularity was used to assess nuclear shape (Circularity = $4 \times \pi \times$ Area / Perimeter^2) with values ranging from 0 (highly irregular shapes) to 1 (perfect circles). Nuclear alignment was assessed by measuring the angle between the μPC axis and the major axis of each nucleus. Cell density was determined based on the number of nuclei detected within each region of interest.

Representative images in the main figures show either HUVECs or hCMEC/D3 cells, with the specific endothelial cell type labeled in each figure. Corresponding images of the other cell type are provided in the supplementary figures.

4.14 | Statistical Analysis

All data were analyzed using R (R Core Team, 2023) via RStudio. For each independent experiment (biological replicate), multiple measurements were obtained when possible. The number of replicates (n), indicated in the figure legends, corresponds to the number of independent experiments. Measurements were averaged within each replicate, and statistical comparisons were performed on these replicate means. Specifically, for nuclear analyses, 330–1712 nuclei were analyzed per experiment. For mean fluorescence intensity (MFI) quantifications, 1–5 images were analyzed for each condition in each experiment depending on image quality, and for layer thickness measurements, 10–24 positions were analyzed per experiment.

Statistical comparisons between conditions were performed on replicate means using paired t-tests, as conditions were matched within the same biological replicate. Given the modest number of independent experiments, formal normality testing was not performed, since such tests have limited power at low sample sizes. Paired t-tests were applied under the assumption of approximate normality.

All plots were generated using the ggplot2 package [91]. In the reported plots, the mean value for each biological replicate (experiment) is shown as a point, with lines connecting paired conditions to highlight matched experimental comparisons. Solid lines represent experiments with HUVECs, whereas dashed lines indicate experiments with hCMEC/D3 endothelial cells. Violin plots display the distribution of individual measurements for large datasets. Boxplots display the median and interquartile range (IQR), with whiskers extending to 1.5× IQR. P-values are indicated on each graph, and the number of biological replicates (n) as well as the number of technical replicates (measurements) are reported in the figure legends.

Acknowledgements

The authors acknowledge the support of the Neuro-oncology team at Erasmus Medical Center (EMC) and the Precision and Microsystems Engineering Laboratory staff, as well as the Nanoscribe team at Delft University of Technology (TU Delft). We are grateful to Franziska Linke, Ruben Bierings, and Iris van Moort for valuable advice on HUVEC culture procedures and for providing the initial batch of cells used during the early planning of the project. We are thankful to Annet Wierenga-Wolf for her valuable support with hCMEC/D3 culture procedures. We thank Pieter van Altena (Department of Precision and Microsystems Engineering, TU Delft) for providing the 3D printed microfluidic chip holder used in the Nanoscribe setup. We are also grateful to Prof. Robbert Rottier (Department of Pediatric Surgery, EMC) for insightful discussions on microfluidic setup design and for providing access to professional-grade cleaning solutions for microfluidic devices. The authors acknowledge financial support from the Nederlandse Organisatie voor Wetenschappelijk Onderzoek (NWO), Grant No. OCENW.XS23.2.105.

Funding

This research was funded by the NWO (Nederlandse Organisatie voor Wetenschappelijk Onderzoek) Grant No. OCENW.XS23.2.105.

Conflicts of Interest

The authors declare no conflicts of interest.

Data Availability Statement

The data that support the findings of this study are available from the corresponding author upon reasonable request.

References

1. H. Zhu, C. Allwin, M. G. Bassous, and A. N. Pouliopoulos, "Focused Ultrasound-Mediated Enhancement of Blood–Brain Barrier Permeability for Brain Tumor Treatment: A Systematic Review of Clinical Trials," *Journal of Neuro-Oncology* 170 (2024): 235–252, https://doi.org/10.1007/s11060-024-04795-z.

2. M. J. van den Bent, M. Geurts, P. J. French, et al., "Primary Brain Tumours in Adults," *The Lancet* 402 (2023): 1564–1579, https://doi.org/10.1016/S0140-6736(23)01054-1.

3. T. C. Hirst, E. Wilson, D. Browne, and E. S. Sena, "A Machine Learning–Assisted Systematic Review of Preclinical Glioma Modeling: Is Practice Changing with the Times?," *Neuro-Oncology Advances* 6 (2024): vdae193, https://doi.org/10.1093/noajnl/vdae193.

4. P. S. Steeg, "The Blood–Tumour Barrier in Cancer Biology and Therapy," *Nature Reviews Clinical Oncology* 18 (2021): 696–714, https://doi.org/10.1038/s41571-021-00529-6.

5. C. D. Arvanitis, G. B. Ferraro, and R. K. Jain, "The Blood–Brain Barrier and Blood–Tumour Barrier in Brain Tumours and Metastases," *Nature Reviews Cancer* 20 (2020): 26–41, https://doi.org/10.1038/s41568-019-0205-x.

6. D. C. Wu, Q. Chen, X. Han, F. Chen, and Z. Wang, "The Blood–Brain Barrier: Structure, Regulation and Drug Delivery," *Signal Transduction and Targeted Therapy* 8 (2023): 217, https://doi.org/10.1038/s41392-023-01481-w.

7. B. T. Hawkins and T. P. Davis, "The Blood–Brain Barrier/Neurovascular Unit in Health and Disease," *Pharmacological Reviews* 57 (2005): 173–185, https://doi.org/10.1124/pr.57.2.4.

8. S. J. Pfau, U. H. Langen, T. M. Fisher, et al., "Characteristics of Blood–Brain Barrier Heterogeneity between Brain Regions Revealed by Profiling Vascular and Perivascular Cells," *Nature Neuroscience* 27 (2024): 1892–1903, https://doi.org/10.1038/s41593-024-01743-y.

9. B. Obermeier, R. Daneman, and R. M. Ransohoff, "Development, Maintenance and Disruption of the Blood-Brain Barrier," *Nature Medicine* 19 (2013): 1584–1596, https://doi.org/10.1038/nm.3407.

10. N. J. Abbott, A. A. K. Patabendige, D. E. M. Dolman, S. R. Yusof, and D. J. Begley, "Structure and Function of the Blood–Brain Barrier," *Neurobiology of Disease* 37 (2010): 13–25, https://doi.org/10.1016/j.nbd.2009.07.030.

11. W. M. Pardridge, "The Blood-Brain Barrier: Bottleneck in Brain Drug Development," *NeuroRX* 2 (2005): 3–14, https://doi.org/10.1602/neurorx.2.1.3.

12. F. Mo, A. Pellerino, R. Soffietti, and R. Rudà, "Blood–Brain Barrier in Brain Tumors: Biology and Clinical Relevance," *International Journal of Molecular Sciences* 22 (2021): 12654, https://doi.org/10.3390/ijms222312654.

13. L. L. Muldoon, J. I. Alvarez, D. J. Begley, et al., "Immunologic Privilege in the Central Nervous System and the Blood–Brain Barrier," *Journal of Cerebral Blood Flow & Metabolism* 33 (2013): 13–21, https://doi.org/10.1038/jcbfm.2012.153.

14. M. H. Ser, M. J. Webb, U. Sener, and J. L. Campian, "Immune Checkpoint Inhibitors and Glioblastoma: A Review on Current State and Future Directions," *Journal of Immunotherapy and Precision Oncology* 7 (2024): 97–110, https://doi.org/10.36401/JIPO-23-34.

15. Y. Hoogstrate, K. Draaisma, S. A. Ghisai, et al., "Transcriptome Analysis Reveals Tumor Microenvironment Changes in Glioblastoma," *Cancer Cell* 41 (2023): 678–692, https://doi.org/10.1016/j.ccell.2023.02.019.

16. M. G. McCoy, D. Nyanyo, C. K. Hung, et al., "Endothelial Cells Promote 3D Invasion of GBM by IL-8–Dependent Induction of Cancer Stem Cell Properties," *Scientific Reports* 9 (2019): 9069, https://doi.org/10.1038/s41598-019-45535-y.

17. E. Testa, C. Palazzo, R. Mastrantonio, and M. T. Viscomi, "Dynamic Interactions between Tumor Cells and Brain Microvascular Endothelial Cells in Glioblastoma," *Cancers* 14 (2022): 3128, https://doi.org/10.3390/cancers14133128.

18. Q. Akolawala, F. Keuning, M. Rovituso, et al., "Micro-Vessels–Like 3D Scaffolds for Studying the Proton Radiobiology of Glioblastoma–Endothelial Cells Co-Culture Models," *Advanced Healthcare Materials* 13 (2024): 2302988, https://doi.org/10.1002/adhm.202302988.

19. T. Wälchli, M. Ghobrial, M. Schwab, et al., "Single-Cell Atlas of the Human Brain Vasculature across Development, Adulthood and Disease," *Nature* 632 (2024): 603–613, https://doi.org/10.1038/s41586-024-07493-y.

20. G. P. Cribaro, E. Saavedra-López, L. Romarate, et al., "Three-Dimensional Vascular Microenvironment Landscape in Human Glioblastoma," *Acta Neuropathologica Communications* 9 (2021): 24, https://doi.org/10.1186/s40478-020-01115-0.

21. H. Wolburg, K. Wolburg-Buchholz, J. Kraus, et al., "Localization of Claudin-3 in Tight Junctions of the Blood-Brain Barrier Is Selectively Lost during Experimental Autoimmune Encephalomyelitis and Human Glioblastoma Multiforme," *Acta Neuropathologica* 105 (2003): 586–592, https://doi.org/10.1007/s00401-003-0688-z.

22. S. Liebner, A. Fischmann, G. Rascher, et al., "Claudin-1 and Claudin-5 Expression and Tight Junction Morphology Are Altered in Blood Vessels of Human Glioblastoma Multiforme," *Acta Neuropathologica* 100 (2000): 323–331, https://doi.org/10.1007/s004010000180.

23. B. Chaulagain, A. Gothwal, R. N. L. Lamptey, et al., "Experimental Models of in Vitro Blood–Brain Barrier for CNS Drug Delivery: an Evolutionary Perspective," *International Journal of Molecular Sciences* 24 (2023): 2710, https://doi.org/10.3390/ijms24032710.

24. S. Kawakita, K. Mandal, L. Mou, et al., "Organ-On-A-Chip Models of the Blood–Brain Barrier: Recent Advances and Future Prospects," *Small* 18 (2022): 2201401, https://doi.org/10.1002/smll.202201401.

25. S. Santaguida, D. Janigro, M. Hossain, E. Oby, E. Rapp, and L. Cucullo, "Side by Side Comparison between Dynamic versus Static Models of Blood–Brain Barrier in Vitro: A Permeability Study," *Brain Research* 1109 (2006): 1–13, https://doi.org/10.1016/j.brainres.2006.06.027.

26. S. Raut, A. Bhalerao, B. Noorani, and L. Cucullo, "In Vitro Models of the Blood–Brain Barrier," *Methods in Molecular Biology* (2022): 25–49, https://doi.org/10.1007/978-1-0716-2289-6_2.

27. G. D. Vatine, R. Barrile, M. J. Workman, et al., "Human iPSC-Derived Blood-Brain Barrier Chips Enable Disease Modeling and Personalized Medicine Applications," *Cell Stem Cell* 24 (2019): 995–1005, https://doi.org/10.1016/j.stem.2019.05.011.

28. T.-E. Park, N. Mustafaoglu, A. Herland, et al., "Hypoxia-Enhanced Blood-Brain Barrier Chip Recapitulates Human Barrier Function and Shuttling of Drugs and Antibodies," *Nature Communications* 10 (2019): 2621, https://doi.org/10.1038/s41467-019-10588-0.

29. M. Zakharova, M. A. Palma do Carmo, M. W. van der Helm, et al., "Multiplexed Blood–Brain Barrier Organ-On-Chip," *Lab on a Chip 20* 20 (2020): 3132–3143, https://doi.org/10.1039/D0LC00399A.

30. T. B. Terrell-Hall, A. G. Ammer, J. I. G. Griffith, and P. R. Lockman, "Permeability across a Novel Microfluidic Blood-Tumor Barrier Model," *Fluids and Barriers of the CNS* 14 (2017): 3, https://doi.org/10.1186/s12987-017-0050-9.

31. M. E. Katt and E. V. Shusta, "Vitro Models of the Blood-Brain Barrier: Building in Physiological Complexity," *Current Opinion in Chemical Engineering* 30 (2020): 42–52, https://doi.org/10.1016/j.coche.2020.07.002.

32. R. Booth and H. Kim, "Permeability Analysis of Neuroactive Drugs through a Dynamic Microfluidic in Vitro Blood–Brain Barrier Model," *Annals of Biomedical Engineering* 42 (2014): 2379–2391, https://doi.org/10.1007/s10439-014-1086-5.

33. J. G. DeStefano, J. J. Jamieson, R. M. Linville, and P. C. Searson, "Benchmarking in Vitro Tissue-Engineered Blood–Brain Barrier Models," *Fluids and Barriers of the CNS* 15 (2018): 32, https://doi.org/10.1186/s12987-018-0117-2.

34. R. Saiga, M. Uesugi, A. Takeuchi, et al., "Brain Capillary Structures of Schizophrenia Cases and Controls Show a Correlation with Their Neuron Structures," *Scientific Reports* 11 (2021): 11768, https://doi.org/10.1038/s41598-021-91233-z.

35. F. Lauwers, F. Cassot, V. Lauwers-Cances, P. Puwanarajah, and H. Duvernoy, "Morphometry of the Human Cerebral Cortex Microcirculation: General Characteristics and Space-Related Profiles," *NeuroImage* 39 (2008): 936–948, https://doi.org/10.1016/j.neuroimage.2007.09.024.

36. F. Cassot, F. Lauwers, C. Fouard, S. Prohaska, and V. Lauwers-Cances, "A Novel Three-Dimensional Computer-Assisted Method for a Quantitative Study of Microvascular Networks of the Human Cerebral Cortex," *Microcirculation* 13 (2006): 1–18, https://doi.org/10.1080/10739680500383407.

37. A. Marino, O. Tricinci, M. Battaglini, et al., "A 3D Real-Scale, Biomimetic, and Biohybrid Model of the Blood–Brain Barrier Fabricated through Two-Photon Lithography," *Small* 14 (2018): 1702959, https://doi.org/10.1002/smll.201702959.

38. C. Hajal, G. S. Offeddu, Y. Shin, et al., "Engineered Human Blood–Brain Barrier Microfluidic Model for Vascular Permeability Analyses," *Nature Protocols* 17 (2022): 95–128, https://doi.org/10.1038/s41596-021-00635-w.

39. S. Bang, S.-R. Lee, J. Ko, et al., "A Low Permeability Microfluidic Blood-Brain Barrier Platform with Direct Contact between Perfusable Vascular Network and Astrocytes," *Scientific Reports* 7 (2017): 8083, https://doi.org/10.1038/s41598-017-07416-0.

40. L. Guida, M. Cavallaro, and M. Levi, "Advancements in High-Resolution 3D Bioprinting: Exploring Technological Trends, Bioinks and

Achieved Resolutions," *Bioprinting* 44 (2024): 00376, https://doi.org/10.1016/j.bprint.2024.e00376.

41. A. P. Dhand, M. D. Davidson, and J. A. Burdick, "Lithography-Based 3D Printing of Hydrogels," *Nature Reviews Bioengineering* 3 (2024): 108–125, https://doi.org/10.1038/s44222-024-00251-9.

42. X. Jing, H. Fu, B. Yu, M. Sun, and L. Wang, "Two-Photon Polymerization for 3D Biomedical Scaffolds: Overview and Updates," *Frontiers in Bioengineering and Biotechnology* 10 (2022): 994355, https://doi.org/10.3389/fbioe.2022.994355.

43. P. F. J. van Altena, L. Castillo Ransanz, M. Manco, V. M. Heine, and A. Accardo, "Micro-Digital Light Processing of Conventional and Hollow Gyroid Mesoscale Hydrogel Scaffolds for Neural Cell Cultures," *Micro and Nano Engineering* 28 (2025): 100310, https://doi.org/10.1016/j.mne.2025.100310.

44. E. Yarali, M. Klimopoulou, K. David, et al., "Bone Cell Response to Additively Manufactured 3D Micro-Architectures with Controlled Poisson's Ratio: Auxetic vs. Non-Auxetic Meta-Biomaterials," *Acta Biomaterialia* 177 (2024): 228–242, https://doi.org/10.1016/j.actbio.2024.01.045.

45. G. Flamourakis, Q. Dong, D. Kromm, et al., "Deciphering the Influence of Effective Shear Modulus on Neuronal Network Directionality and Growth Cones' Morphology via Laser-Assisted 3D-Printed Nanostructured Arrays," *Advanced Functional Materials* 35 (2025): 2409451, https://doi.org/10.1002/adfm.202409451.

46. E. D. S. Lemma, B. De Vittorio, and M. Pisanello, "Studying Cell Mechanobiology in 3D: the Two-Photon Lithography Approach," *Trends in Biotechnology* 37 (2019): 358–372, https://doi.org/10.1016/j.tibtech.2018.09.008.

47. N. Barin, H. E. Balcioglu, I. de Heer, et al., "3D-Engineered Scaffolds to Study Microtubes and Localization of Epidermal Growth Factor Receptor in Patient-Derived Glioma Cells," *Small* 18 (2022): 2204485, https://doi.org/10.1002/smll.202204485.

48. Q. Akolawala, M. Rovituso, H. H. Versteeg, A. M. R. Rondon, and A. Accardo, "Evaluation of Proton-Induced DNA Damage in 3D-Engineered Glioblastoma Microenvironments," *ACS Applied Materials & Interfaces* 14 (2022): 20778–20789, https://doi.org/10.1021/acsami.2c03706.

49. B. B. Weksler, E. A. Subileau, N. Perrière, et al., "Blood–Brain Barrier–Specific Properties of a Human Adult Brain Endothelial Cell Line," *The FASEB Journal* 19 (2005): 1872–1874, https://doi.org/10.1096/fj.04-3458fje.

50. J. T. Flaherty, J. E. Pierce, V. J. Ferrans, D. J. Patel, W. K. Tucker, and D. L. Fry, "Endothelial Nuclear Patterns in the Canine Arterial Tree with Particular Reference to Hemodynamic Events," *Circulation Research* 30 (1972): 23–33, https://doi.org/10.1161/01.RES.30.1.23.

51. A. D. Stephens, E. J. Banigan, and J. F. Marko, "Chromatin's Physical Properties Shape the Nucleus and Its Functions," *Current Opinion in Cell Biology* 58 (2019): 76–84, https://doi.org/10.1016/j.ceb.2019.02.006.

52. B. M. Skinner and E. E. P. Johnson, "Nuclear Morphologies: Their Diversity and Functional Relevance," *Chromosoma* 126 (2017): 195–212, https://doi.org/10.1007/s00412-016-0614-5.

53. A. L. Hazel and T. J. Pedley, "Vascular Endothelial Cells Minimize the Total Force on Their Nuclei," *Biophysical Journal* 78 (2000): 47–54, https://doi.org/10.1016/S0006-3495(00)76571-4.

54. B. L. Langille and S. L. Adamson, "Relationship between Blood Flow Direction and Endothelial Cell Orientation at Arterial Branch Sites in Rabbits and Mice," *Circulation Research* 48 (1981): 481–488, https://doi.org/10.1161/01.RES.48.4.481.

55. A. R. Bond, C.-W. Ni, H. Jo, and P. D. Weinberg, "Intimal Cushions and Endothelial Nuclear Elongation around Mouse Aortic Branches and Their Spatial Correspondence with Patterns of Lipid Deposition," *American Journal of Physiology–Heart and Circulatory Physiology* 298 (2010): H536–H544, https://doi.org/10.1152/ajpheart.00917.2009.

56. C. F. Dewey, S. R. Bussolari, M. A. Gimbrone, and P. F. Davies, "The Dynamic Response of Vascular Endothelial Cells to Fluid Shear Stress," *Journal of Biomechanical Engineering* 103 (1981): 177–185, https://doi.org/10.1115/1.3138276.

57. J. R. Privratsky and P. J. Newman, "PECAM-1: Regulator of Endothelial Junctional Integrity," *Cell and Tissue Research* 355 (2014): 607–619, https://doi.org/10.1007/s00441-013-1779-3.

58. A.-C. Luissint, C. Artus, F. Glacial, K. Ganeshamoorthy, and P.-O. Couraud, "Tight Junctions at the Blood Brain Barrier: Physiological Architecture and Disease-Associated Dysregulation," *Fluids and Barriers of the CNS* 9 (2012): 23, https://doi.org/10.1186/2045-8118-9-23.

59. S. M. Stamatovic, A. M. Johnson, R. F. Keep, and A. V. Andjelkovic, "Junctional Proteins of the Blood-Brain Barrier: New Insights into Function and Dysfunction," *Tissue Barriers* 4 (2016): 1154641, https://doi.org/10.1080/21688370.2016.1154641.

60. S. R. Archie, A. Al Shoyaib, and L. Cucullo, "Blood-Brain Barrier Dysfunction in CNS Disorders and Putative Therapeutic Targets: An Overview," *Pharmaceutics* 13 (2021): 1779, https://doi.org/10.3390/pharmaceutics13111779.

61. K. D. Rochfort, L. E. Collins, R. P. Murphy, and P. M. Cummins, "Downregulation of Blood–Brain Barrier Phenotype by Proinflammatory Cytokines Involves NADPH Oxidase–Dependent ROS Generation: Consequences for Interendothelial Adherens and Tight Junctions," *PLoS ONE* 9 (2014): 101815, https://doi.org/10.1371/journal.pone.0101815.

62. A. S. Şovrea, B. Boşca, C. S. Melincovici, et al., "Multiple Faces of the Glioblastoma Microenvironment," *International Journal of Molecular Sciences* 23 (2022): 595, https://doi.org/10.3390/ijms23020595.

63. Y. Feng, J. Wang, D. Tan, P. Cheng, and A. Wu, "Relationship between Circulating Inflammatory Factors and Glioma Risk and Prognosis: a Meta-Analysis," *Cancer Medicine* 8 (2019): 7454–7468, https://doi.org/10.1002/cam4.2585.

64. T. Liu, L. Zhang, D. Joo, and S.-C. Sun, "NF-κB Signaling in Inflammation," *Signal Transduction and Targeted Therapy* 2 (2017): 17023, https://doi.org/10.1038/sigtrans.2017.23.

65. J.-Y. Lee and C. Y. Kim, "Preventive Effects of Thinned Apple Extracts on TNF-α–Induced Intestinal Tight Junction Dysfunction in Caco-2 Cells through Myosin Light Chain Kinase Suppression," *Foods* 11 (2022): 1714, https://doi.org/10.3390/foods11121714.

66. H. Wang, X. Mao, L. Ye, H. Cheng, and X. Dai, "The Role of the S100 Protein Family in Glioma," *Journal of Cancer* 13 (2022): 3022–3030, https://doi.org/10.7150/jca.73365.

67. R. Uceda-Castro, J. V. van Asperen, C. Vennin, et al., "GFAP Splice Variants Fine-Tune Glioma Cell Invasion and Tumour Dynamics by Modulating Migration Persistence," *Scientific Reports* 12 (2022): 424, https://doi.org/10.1038/s41598-021-04127-5.

68. C. Wang, J. Li, S. Sinha, A. Peterson, G. A. Grant, and F. Yang, "Mimicking Brain Tumor-Vasculature Microanatomical Architecture via Co-Culture of Brain Tumor and Endothelial Cells in 3D Hydrogels," *Biomaterials* 202 (2019): 35–44, https://doi.org/10.1016/j.biomaterials.2019.02.024.

69. C. Charalambous, F. M. Hofman, and T. C. Chen, "Functional and Phenotypic Differences between Glioblastoma Multiforme–Derived and Normal Human Brain Endothelial Cells," *Journal of Neurosurgery* 102 (2005): 699–705, https://doi.org/10.3171/jns.2005.102.4.0699.

70. E. di Tomaso, D. Capen, A. Haskell, et al., "Mosaic Tumor Vessels: Cellular Basis and Ultrastructure of Focal Regions Lacking Endothelial Cell Markers," *Cancer Research* 65 (2005): 5740–5749, https://doi.org/10.1158/0008-5472.CAN-04-4552.

71. E. K. Bosma, C. J. F. van Noorden, R. O. Schlingemann, and I. Klaassen, "The Role of Plasmalemma Vesicle-Associated Protein in Pathological Breakdown of Blood–Brain and Blood–Retinal Barriers: Potential Novel Therapeutic Target for Cerebral Edema and Diabetic Macular Edema," *Fluids and Barriers of the CNS* 15 (2018): 24, https://doi.org/10.1186/s12987-018-0109-2.

72. E. A. Winkler, R. D. Bell, and B. V. Zlokovic, "Central Nervous System Pericytes in Health and Disease," *Nature Neuroscience* 14 (2011): 1398–1405, https://doi.org/10.1038/nn.2946.

73. H. Gerhardt and C. Betsholtz, "Endothelial–Pericyte Interactions in Angiogenesis," *Cell and Tissue Research* 314 (2003): 15–23, https://doi.org/10.1007/s00441-003-0745-x.

74. G. Li, J. Gao, P. Ding, and Y. Gao, "The Role of Endothelial Cell–Pericyte Interactions in Vascularization and Diseases," *Journal of Advanced Research* 67 (2025): 269–288, https://doi.org/10.1016/j.jare.2024.01.016.

75. G. Allt and J. G. Lawrenson, "Pericytes: Cell Biology and Pathology," *Cells Tissues Organs* 169 (2001): 1–11, https://doi.org/10.1159/000047855.

76. A. Farin, S. O. Suzuki, M. Weiker, J. E. Goldman, J. N. Bruce, and P. Canoll, "Transplanted Glioma Cells Migrate and Proliferate on Host Brain Vasculature: a Dynamic Analysis," *Glia* 53 (2006): 799–808, https://doi.org/10.1002/glia.20334.

77. G. Seano and R. K. Jain, "Vessel Co-Option in Glioblastoma: Emerging Insights and Opportunities," *Angiogenesis* 23 (2020): 9–16, https://doi.org/10.1007/s10456-019-09691-z.

78. E. Mairey, A. Genovesio, E. Donnadieu, et al., "Cerebral Microcirculation Shear Stress Levels Determine *Neisseria meningitidis* Attachment Sites along the Blood–Brain Barrier," *The Journal of Experimental Medicine* 203 (2006): 1939–1950, https://doi.org/10.1084/jem.20060482.

79. E. R. Damiano, J. Westheider, A. Tözeren, and K. Ley, "Variation in the Velocity, Deformation, and Adhesion Energy Density of Leukocytes Rolling within Venules," *Circulation Research* 79 (1996): 1122–1130, https://doi.org/10.1161/01.RES.79.6.1122.

80. R. S. Reneman and A. P. G. Hoeks, "Wall Shear Stress as Measured in Vivo: Consequences for the Design of the Arterial System," *Medical & Biological Engineering & Computing* 46 (2008): 499–507, https://doi.org/10.1007/s11517-008-0330-2.

81. O. Tricinci, D. De Pasquale, A. Marino, M. Battaglini, C. Pucci, and G. Ciofani, "A 3D Biohybrid Real-Scale Model of the Brain Cancer Microenvironment for Advanced in Vitro Testing," *Advanced Materials Technologies* 5 (2020), https://doi.org/10.1002/admt.202000540.

82. M. S. Thomsen, L. J. Routhe, and T. Moos, "The Vascular Basement Membrane in the Healthy and Pathological Brain," *Journal of Cerebral Blood Flow & Metabolism* 37 (2017): 3300–3317, https://doi.org/10.1177/0271678X17722436.

83. L. Jiang, S. Li, J. Zheng, Y. Li, and H. Huang, "Recent Progress in Microfluidic Models of the Blood-Brain Barrier," *Micromachines* 10 (2019): 375, https://doi.org/10.3390/mi10060375.

84. Y. I. Wang, H. E. Abaci, and M. L. Shuler, "Microfluidic Blood–Brain Barrier Model Provides in Vivo–Like Barrier Properties for Drug Permeability Screening," *Biotechnology and Bioengineering* 114 (2017): 184–194, https://doi.org/10.1002/bit.26045.

85. M. W. van der Helm, A. D. van der Meer, J. C. T. Eijkel, A. van den Berg, and L. I. Segerink, "Microfluidic Organ-on-Chip Technology for Blood-Brain Barrier Research," *Tissue Barriers* 4 (2016): 1142493, https://doi.org/10.1080/21688370.2016.1142493.

86. B. Srinivasan, A. R. Kolli, M. B. Esch, H. E. Abaci, M. L. Shuler, and J. J. Hickman, "TEER Measurement Techniques for in Vitro Barrier Model Systems," *SLAS Technology* 20 (2015): 107–126, https://doi.org/10.1177/2211068214561025.

87. M. Odijk, A. D. van der Meer, D. Levner, et al., "Measuring Direct Current Trans-Epithelial Electrical Resistance in Organ-on-a-Chip Microsystems," *Lab on a Chip* 15 (2015): 745–752, https://doi.org/10.1039/C4LC01219D.

88. F. Sivandzade and L. Cucullo, "In-Vitro Blood–Brain Barrier Modeling: a Review of Modern and Fast-Advancing Technologies," *Journal of Cerebral Blood Flow & Metabolism* 38 (2018): 1667–1681, https://doi.org/10.1177/0271678X18788769.

89. A. Sharaf, B. Roos, R. Timmerman, G.-J. Kremers, J. J. Bajramovic, and A. Accardo, "Two-Photon Polymerization of 2.5D and 3D Microstructures Fostering a Ramified Resting Phenotype in Primary Microglia," *Frontiers in Bioengineering and Biotechnology* 10 (2022): 926642, https://doi.org/10.3389/fbioe.2022.926642.

90. U. Schmidt, M. Weigert, C. Broaddus, and G. Myers, "Cell Detection with Star-Convex Polygons," Lecture Notes in Computer Science (including subseries Lecture Notes in Artificial Intelligence and Lecture Notes in Bioinformatics) 11071 (2018): 265–273, https://doi.org/10.1007/978-3-030-00934-2_30.

91. H. Wickham, *Ggplot2, Use R! Series* (Springer International Publishing, 2016), https://doi.org/10.1007/978-3-319-24277-4.

Supporting Information

Additional supporting information can be found online in the Supporting Information section.

Supporting File 1: admt70712-sup-0001-SuppMat.pdf.

Supporting File 2: admt70712-sup-0002-VideoS1.mp4.

Supporting File 3: admt70712-sup-0003-VideoS2.mp4.